Global and Planetary Change 204 (2021) 103581

Contents lists available at ScienceDirect

Global and Planetary Change

journal homepage: www.elsevier.com/locate/gloplacha

Eocene-Oligocene paleoenvironmental changes in the South Orkney Microcontinent (Antarctica) linked to the opening of Powell Basin

Adrián López-Quirós[a,b,*], Carlota Escutia[b], Johan Etourneau[b,c,d], Francisco J. Rodríguez-Tovar[e], Sabine Roignant[f], Francisco J. Lobo[b], Nick Thompson[g], Peter K. Bijl[h], Fernando Bohoyo[i], Ulrich Salzmann[g], Dimitris Evangelinos[b], Ariadna Salabarnada[b], Frida S. Hoem[h], Marie-Alexandrine Sicre[f]

[a] *Department of Geoscience, Aarhus University, Høegh-Guldbergs Gade 2, 8000 Aarhus C, Denmark*
[b] *Instituto Andaluz de Ciencias de la Tierra, CSIC-Universidad de Granada, Avda. de las Palmeras 4, 18100, Armilla, Granada, Spain*
[c] *EPHE, PSL Research University, Paris, France*
[d] *UMR 5805 EPOC CNRS, University of Bordeaux, Bordeaux, France*
[e] *Department of Stratigraphy and Paleontology, University of Granada, 18071 Granada, Spain*
[f] *UMR 7159 LOCEAN CNRS-IRD-MNHN, Sorbonne Universités, Paris, France*
[g] *Department of Geography and Environmental Sciences, Northumbria University, Newcastle upon Tyne, UK*
[h] *Department of Earth Science, Utrecht University, Budapestlann 4, 3584 CB Utrecht, the Netherlands*
[i] *Instituto Geológico y Minero de España, Rios Rosas 23, 28003 Madrid, Spain*

ARTICLE INFO

Keywords:
Late Eocene-early Oligocene
Drake Passage
South Orkney Microcontinent
ODP 696
Paleoenvironment

ABSTRACT

The scarcity of paleo-records from the Antarctic Peninsular region of the Southern Ocean hinders our understanding of the timing of the opening of Drake Passage, specifically in the region of the South Orkney Microcontinent (SOM) and Powell Basin, between the Scotia and Antarctic plates. At Ocean Drilling Program (ODP) Hole 696B, SOM sediments recovered from the upper Eocene-lower Oligocene (~37.6–32.2 Ma) enable us to gain insight into paleoceanographic and paleoclimatic changes during gateway opening across the major Cenozoic climate shift —the Eocene-Oligocene transition— when the Antarctic ice sheet first reached sea-level. We propose the following sequence of events, based on a multi-proxy analysis of sediment facies, mineralogy, and organic matter geochemistry (TOC, TN, C/N ratio, $\delta^{13}C$, $\delta^{15}N$, and *n*-alkanes).

During the late Eocene (~37.6–35.5 Ma) the SOM was attached to the Antarctic Peninsula, and terrigenous sediments of likely local origin were deposited in shallow waters under conditions of reduced-oxygen/low-salinity, and temperate climate. In the latest Eocene (~35.5–34.1 Ma), terrigenous input was reduced due to the separation of the SOM from the Antarctic Peninsula by proto-Powell Basin opening. Decreased sediment supply during continuous deepening of the SOM led to deposition of a condensed section with significant glauconitization, recurrent winnowing by bottom currents, and suboxic conditions near the sediment-water interface. At the time of the Eocene-Oligocene transition (EOT; ~34.1–33.6 Ma) two upward-coarsening sediment sections were deposited within an overall upward-fining section, which we interpret as records of regressive phases due to ice sheet expansion. During the early Oligocene (~33.6–33.2 Ma) the SOM deepened further because of continued opening of Powell Basin, and organic-rich sediments were deposited as a result of enhanced biological production, partially driven by enhanced upwelling. Major cooling caused a change from forests indicating relatively humid temperate conditions in the late Eocene, to forests indicative of dry and cool conditions in the Oligocene, as shown by biomarker records, which also indicate weakening contributions of terrestrial organic matter to the marine sedimentary record.

We thus conclude that a shallow gateway, the proto-Powell Basin, formed at ~35.5 Ma, as seen in the decreased delivery of proximal, coarse terrigenous sediments to the SOM margin; this was followed by a long-term deepening trend, interrupted by EOT regression due to continent-wide ice sheet build-up. Opening of the proto-Powell Basin could have provided a shallow-water pathway for water flowing from the Drake Passage-Scotia Sea towards the northern Weddell Sea, enhancing upwelling at the southern SOM shelf margin. Hence,

---

[*] Corresponding author at: Department of Geoscience, Aarhus University, Høegh-Guldbergs Gade 2, 8000 Aarhus C, Denmark.
E-mail address: alquiros@geo.au.dk (A. López-Quirós).

https://doi.org/10.1016/j.gloplacha.2021.103581
Received 3 November 2020; Received in revised form 25 June 2021; Accepted 13 July 2021
Available online 18 July 2021
0921-8181/© 2021 Elsevier B.V. All rights reserved.

increased marine productivity across the EOT might have resulted from the combined effects of the opening of Powell Basin and climate cooling.

1. Introduction

The Eocene-Oligocene Transition (EOT), marked by a 1.5‰ positive excursion of $\delta^{18}O$ values in deep-sea benthic foraminifera at 34–33.5 Ma, was a major global climatic event involving cooling, the onset of full-scale glaciation in Antarctica (e.g., Zachos et al., 2001; Coxall et al., 2005; Passchier et al., 2017), progressive global sea-level fall (e.g., Miller et al., 2005; Stocchi et al., 2013), and a global or regional increase in oceanic primary productivity at high southern latitudes (e.g., Egan et al., 2013; Houben et al., 2013; Villa et al., 2014). Geological consequences of the dramatic changes were conspicuous around Antarctica and the Southern Ocean. Middle Eocene sediments in the Antarctic Peninsula region indicate mild, frost-free winters and moisture availability sufficient to support highly diverse subtropical and temperate rain forests (e.g., Mohr, 2001; Poole et al., 2005; Francis et al., 2008). During the late Eocene, from approximately 2 myr before the EOT, large-scale changes in flora composition and diversity recorded the onset of prolonged cooling in the Antarctic Peninsula (e.g., Askin, 2000; Anderson et al., 2011; Warny and Askin, 2011), and associated moisture changes led to periods of drought (Hosking and Hutcheson, 1988; Suarez et al., 2004). Vegetation persisted across the EOT, but the warm Eocene vegetation was replaced by shrubby vegetation (i.e., southern beech *Nothofagus*, mosses and ferns), which could survive in tundra-like conditions (Francis et al., 2009). Another significant change during the EOT was the switch from chemical to physical weathering dominance around Antarctica (e.g., Ehrmann and Mackensen, 1992; Escutia et al., 2011; Basak and Martin, 2013; Passchier et al., 2013). Offshore, the arrival of ice sheets at the Antarctic continental margins was recorded by deposition of subglacial and ice-proximal deposits on the continental shelves, as well as by iceberg transport and delivery of Ice Rafted Debris (IRD) to the seabed all around Antarctica (e.g., Barker et al., 1988 for the Weddell Sea; Passchier and Krissek, 2008 for the Ross Sea; Escutia et al., 2011, 2014 for Wilkes Land).

The opening and deepening of the Tasmania and Drake oceanic passages has been invoked as the cause of these major climatic changes, by enabling the exchange of water masses between the Atlantic, Indian and Pacific oceans in the Antarctic Circumpolar Current (ACC) (e.g., Kennett, 1977; Lawver and Gahagan, 1998; Exon et al., 2001), implying the thermal isolation of Antarctica and ultimately growth of its massive ice sheets. A major drawback to this hypothesis is that the timing of Drake Passage's opening and deepening remains highly controversial, with potential timing from the Eocene to the Miocene (e.g., Barker and Burrell, 1977; Barker, 2001; Lawver and Gahagan, 2003; Barker and Thomas, 2004; Livermore et al., 2004, 2007; Eagles et al., 2006; Scher and Martin, 2006; Cramer et al., 2009; Lagabrielle et al., 2009; Maldonado et al., 2014). Thus we cannot independently link the formation of ocean gateways, the development of a modern-like ACC, and the establishment of the Antarctic ice sheet. The opening of Powell Basin was part of a regional response to relative plate motion of South America away from Antarctica, the ultimate stage of Drake Passage opening (e.g., Eagles and Livermore, 2002; Livermore et al., 2007). The paucity of records and lack of age control hinder not only our understanding of the timing and patterns of Drake Passage opening and deepening, but also of the regional paleoenvironmental and paleoceanographic changes across the EOT. More specifically, questions surround the region of the South Orkney Microcontinent (SOM) and Powell Basin, viewed as an integral part of Drake Passage opening.

Analysis of organic matter in marine sediments provides information widely utilized to evaluate past ocean and continental climates and environmental changes (e.g., Freeman et al., 1994; Meyers, 1997; Muller and Voss, 1999; Ficken et al., 2000; Huon et al., 2002; Schefuß et al., 2003; Lamb et al., 2006; Vogts et al., 2009; Arbi et al., 2018). Organic matter contains some of the longest-living proxies of delivery and accumulation in marine settings, providing information about its sources, nutrient cycling and vegetation, and even depositional conditions. Organic matter is a mixture of molecular compounds of diverse origins, with different degrees of preservation, susceptible to diagenesis and biological alteration during and after sinking to the seafloor and subsequent downslope transport. An integration of geochemical techniques based on determination of elemental and stable isotopic compositions and lipid biomarkers (i.e., total organic carbon/total nitrogen (TOC/TN) ratios, $\delta^{13}C$, $\delta^{15}N$ and molecular *n*-alkanes) is needed to tease out these effects so as to optimize paleoenvironmental and paleoecological reconstructions.

The SOM, located on the South Scotia Ridge (SSR) between the Scotia and Antarctic plates, is a remnant of a former continental link between the Antarctic Peninsula and South America (e.g., Dalziel, 1984; Barker et al., 1991). Availability of a revised age model for Ocean Drilling Program (ODP) Leg 113 Site 696, drilled on the southeastern margin of the SOM (Barker et al., 1988; Houben et al., 2013, 2019), provides an opportunity to evaluate the paleoenvironmental and paleoceanographic changes of the initial phases of opening of Powell Basin, a product of the opening and deepening of the Drake Passage across the EOT. The goals of this study are: (1) to determine the changes in sedimentary environments from the late Eocene to the early Oligocene and their timing (∼37.6–32.2 Ma), potentially linked to the initial phase of separation and deepening of the SOM from the Antarctic Peninsula; (2) to estimate sources (terrestrial vs. marine) of organic matter; (3) to infer paleoclimatic and paleoceanographic processes and their relation to the preservation of organic matter.

2. Geological setting

The SOM is the largest (about 70,000 km^2) continental fragment along the southern boundary of the Scotia Arc (Fig. 1), being a remnant of the land bridge connecting South America and the Antarctic Peninsula prior to the Paleogene continental break-up (Dalziel and Elliot, 1971; de Wit, 1977; Dalziel, 1984; Barker et al., 1991). Estimates of the timing of SOM's break from the Antarctic Peninsula range from the mid-Eocene to the early Oligocene (40–30 Ma; King and Barker, 1988; Coren et al., 1997; Eagles and Livermore, 2002). The SOM drifted and rotated eastward in conjunction with the rifting and subsequent opening of Powell and Jane Basins (King and Barker, 1988; Trouw et al., 1997; Maldonado et al., 1998; Busetti et al., 2000; Bohoyo et al., 2002; Maestro et al., 2013), attaining its current location during the early Miocene (King and Barker, 1988; Coren et al., 1997).

The South Orkney Islands are the only emerged areas (Figs. 1, 2A) by the active northern SOM margin, with outcropping Permian-Triassic sandstones and mudstones (i.e., metapelites and metagreywackes of the Greywacke Shale Formation and the Scotia Metamorphic Complex), interpreted as turbidites (Dalziel, 1984; Flowerdew et al., 2011). The southeast and southwest SOM passive margins are connected to the Powell and Jane oceanic basins, respectively, whereas the southern SOM margin is connected to the oceanic Weddell Basin (King and Barker, 1988; Lawver et al., 1991). The deformational style of the southwestern margin resulted in both steep and gentle slopes, as well as locally detached elevations. In contrast, the southeastern margin is more irregular and less steep overall (King and Barker, 1988).

The SOM has two main structural domains: (1) an older domain characterized by an east-west trend comprising a magmatic arc, a forearc basin filled with up to 5000 m of sediments (the Newton Basin; Fig. 2A), and a Mesozoic accretionary complex, reflecting the location of the SOM on the Pacific margin; and (2) a younger N-S trending domain encompassing three epicontinental basins (Airy, Bouguer and Eötvös; Fig. 2A), with horsts and grabens formed during the Eocene-Oligocene fragmentation of the Scotia Ridge (King and Barker, 1988). According to the ODP stratigraphy (Barker et al., 1988), Eötvös Basin is filled at least by upper Eocene-Quaternary sediments.

3. Materials and methods

3.1. *Site descriptions and age model of ODP Site 696*

At ODP Site 696 (61°50.96′ S, 42°56′ W) two holes were drilled at 650 m water depth in Eötvös Basin, at the southeastern margin of the SOM, northern Weddell Sea (Barker et al., 1988; Fig. 2A). Terrigenous to authigenic sediments (646–530 m below seafloor–mbsf), pelagic sediments (530–214 mbsf), and hemipelagic sediments (214–0 mbsf) were deposited from the late Eocene to the Quaternary (Barker et al., 1988; Gersonde and Burckle, 1990; Wei and Wise, 1990; Fig. 2B). Onboard the ship, the upper Eocene-lower middle Miocene terrigenous to authigenic lithological unit designated as Unit VII (646–530 mbsf) was tentatively subdivided into four subunits (Barker et al., 1988): Subunit VIID (645.6 to 606.9 mbsf), organic-rich sandy mudstone facies; Subunit VIIC (606.9 to 569.7 mbsf), glaucony-bearing packstone facies (Barker et al., 1988; López-Quirós et al., 2019); Subunit VIIB (569.7 to 548.9 mbsf), claystone and limestone facies; and Subunit VIIA (548.9 to 529.8 mbsf), rhythmically interbedded sandy mudstone facies with glauconite-bearing sandstone beds (Barker et al., 1988; López-Quirós et al., 2020). This study focuses on subunits VIID, VIIC and VIIB from Hole 696B, interpreted onboard as deposited in a shallow marine environment (Barker et al., 1988; Fig. 3).

Stratigraphic age control of Subunit VIID was established through calcareous nannofossils (Wei and Wise, 1990 sensu Villa et al., 2008; Fig. 3). The First Consistent Occurrence (FCO) of *Isthmolithus recurvus* (617 mbsf; Wei and Wise, 1990) and the occurrence of *Reticulofenestra bisecta* (643.62 mbsf; Wei and Wise, 1990) places the base at ~36.5 Ma, although the subunit could be as old as 37.6 Ma (Villa et al., 2008). The First Occurrence (FO) of *Reticulofenestra oamaruensis* is recorded at the base of Subunit VIIC (598.42 to 588.72 mbsf; Wei and Wise, 1990), suggesting a maximum age of about 35.5 Ma (Villa et al., 2008). For the overlying sediments (including subunits VIIC and VIIB), a revised dinocyst-based age model gave a late Eocene to early Oligocene age (Houben et al., 2013, 2019) (Fig. 3). The FO of *Stoveracysta kakanuiensis* was calibrated to the latest Eocene (>33.8 Ma) in sediments and rocks from the East Tasman Plateau (ODP Site 1172) and in New Zealand (Clowes, 1985). In ODP Hole 696B, the FO of *S. kakanuiensis* (Houben et al., 2013, 2019) (34.1 Ma; 571.55 mbsf) predates the FO of *Malvinia escutiana*, used as indicator of the Oligocene isotope event 1 (Oi-1; 33.6 Ma) (Houben et al., 2013, 2019) (569.11 mbsf), which suggests that the EOT was well recovered at this site. The FO of the low-latitude taxon *Chiropteridium galea* (<33.26 Ma) (Pross et al., 2010) at 552.2 mbsf (Houben et al., 2019) suggests a quite complete and expanded lowermost Oligocene succession.

3.2. *Methodology and analyses*

The sediments of the interval under consideration were subjected to different types of analyses:

3.2.1. *Facies analyses*

Sediment facies analyses were conducted for the interval ~ 646 mbsf

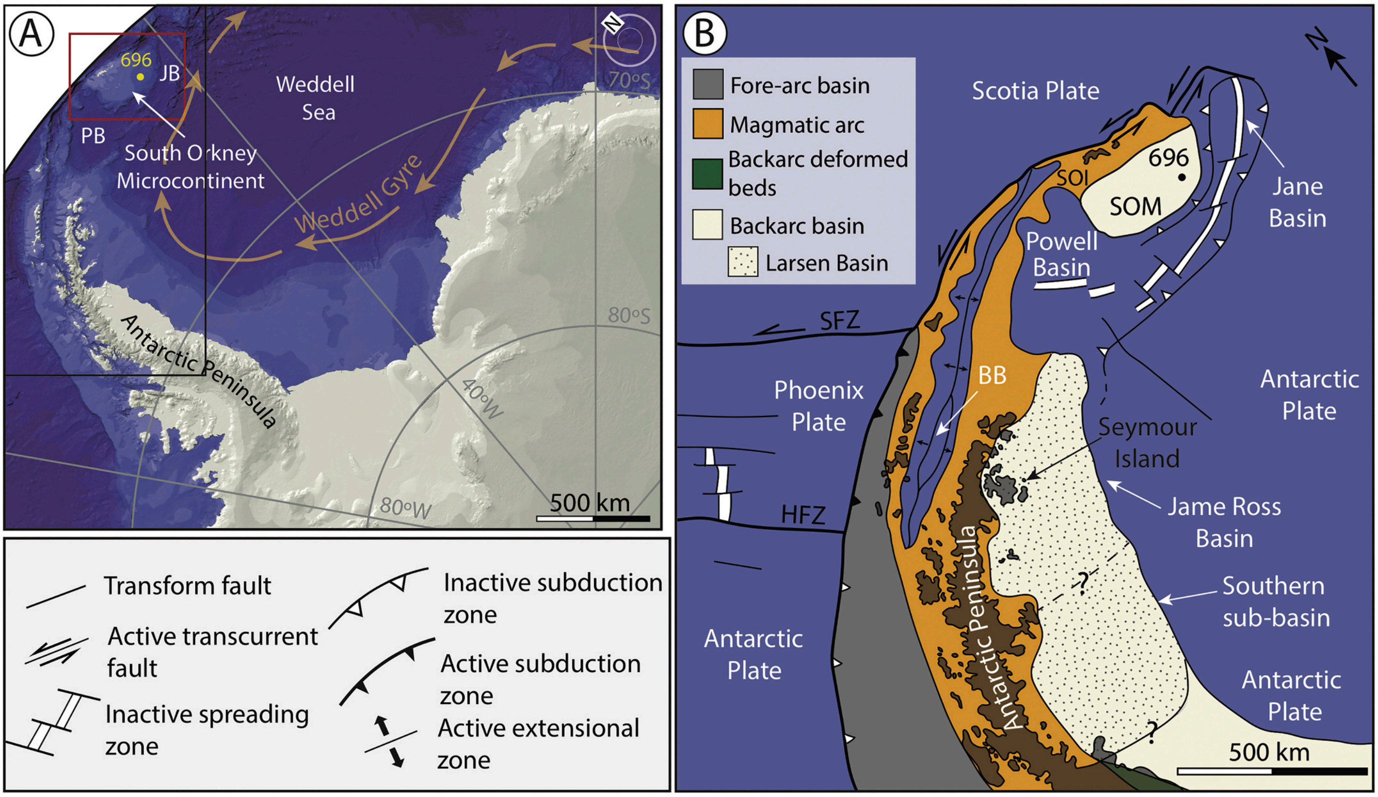

Fig. 1. Geographic and geological setting of the study area. A) Location of Leg 113, ODP Site 696, on the South Orkney Microcontinent (red box). Map from IBCSO v. 1.0 (Arndt et al., 2013). Schematic position of the Weddell Gyre at present (Orsi et al., 1993) is indicated. PB: Powell Basin; JB: Jane Basin. B) Present tectonic setting and litho-tectonic units for the Antarctic Peninsula (modified after Elliot, 1988). Tectonic features after Maldonado et al. (2000, 2014). SOM: South Orkney Microcontinent; SOI: South Orkney Islands; BB: Bransfield Basin; SFZ: Shackleton Fracture Zone; HFZ: Hero Fracture Zone. (For interpretation of the references to colour in this figure legend, the reader is referred to the web version of this article.)

to ~549 mbsf (Fig. 3) to establish a stratigraphic framework and attempt a paleoenvironmental reconstruction. Sediment facies were defined on the basis of visual core descriptions, thin sections and core slabs, expanding on the lower-resolution preliminary shipboard descriptions by Barker et al. (1988).

Macroscopic visual core observations were aided by high-resolution digital images obtained from archive halves using a Nikon 60 mm camera lens mounted on a custom-built line scanner at the Coast Gulf Repository (CGR), Texas A&M University (College Station, Texas, USA). Facies type determination included lithology, sediment textures, grain sizes, sedimentary structures and bioturbation, following Tucker (2001) and references therein. Facies classification is after Dunham (1962) and Mount (1985). Additionally, high-resolution digital images were used for ichnological facies analyses applying a previously established digital procedure (Dorador and Rodríguez-Tovar, 2014, 2018; and references therein). Ichnotaxonomical characterization at the ichnogenus level is based on the recognition of ichnotaxobases in cores (Knaust, 2012, 2017).

Composition of biogenic and terrigenous grains, grain size and shape were determined microscopically using petrographic and environmental scanning electron (ESEM) microscopes. The petrographic characterization was made under polarized and cross-polarized light with an OLYMPUS BX60 microscope at the Instituto Andaluz de Ciencias de la Tierra (CSIC-University of Granada, Spain). Back-scattered electron (BSE) and secondary electron (SE) observations were made with an ESEM FEI Quanta 400 microscope at the Centro de Instrumentación Científica (CIC, University of Granada, Spain).

Bulk grain-size analyses were completed at the Environnements et

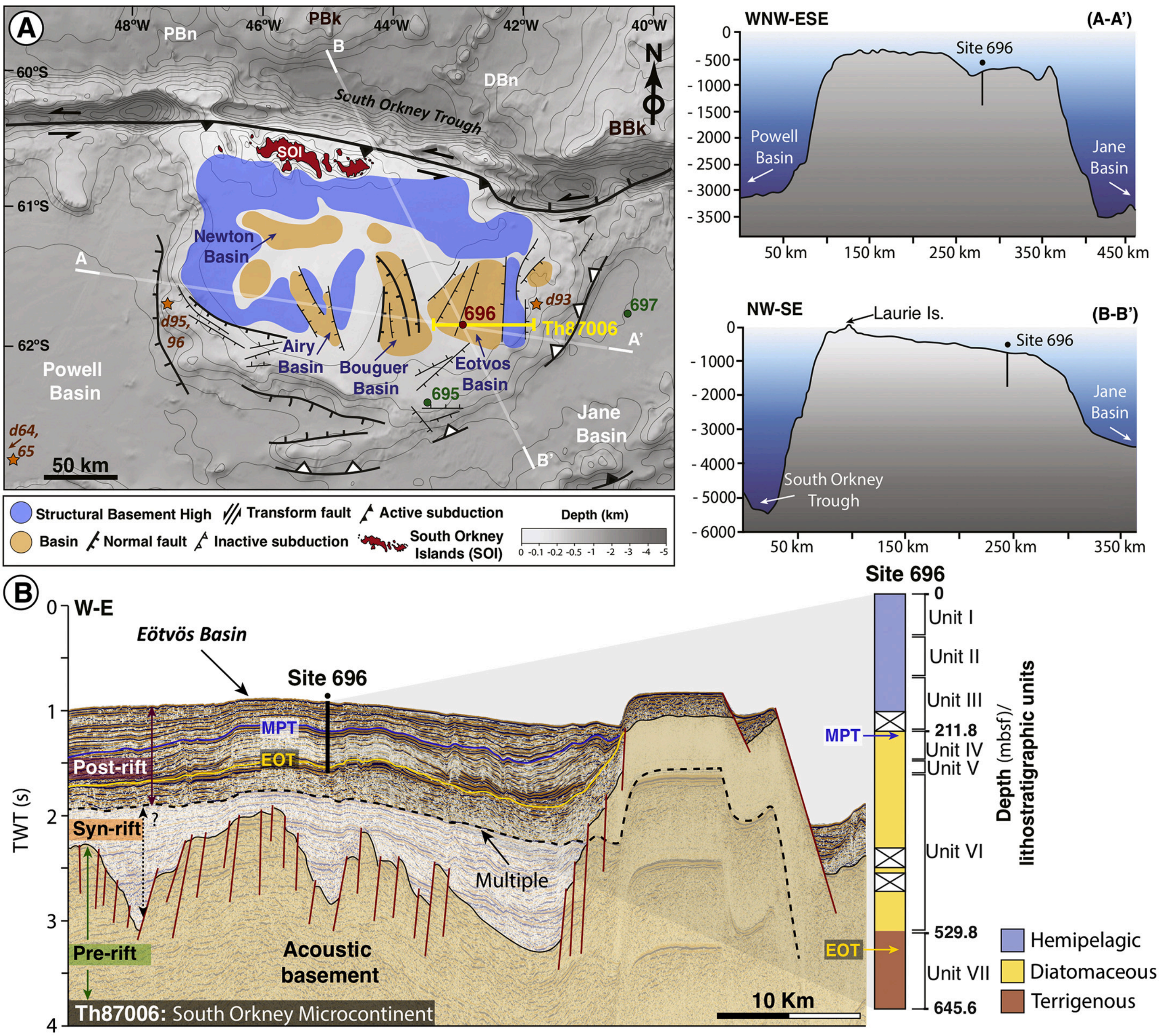

Fig. 2. Geological setting of the South Orkney Microcontinent (SOM). A) Regional bathymetry of the SOM shelf and location of ODP (696, 695 and 697) and dredge sites, with selected bathymetric profiles (A-A' and B-B') and a multichannel seismic line (Th87006). Structural features after Busetti et al. (2000) and King and Barker (1988). Bathymetric map extracted from GEBCO 2014 (NOAA/NCEI). PBn: Protector Basin; PBk: Pirie Bank; DBn: Dove Basin; BBk: Bruce bank. B) Multichannel seismic profile (Th87006; available at the Antarctic Seismic Data Library System: http://sdls.ogs.trieste.it/) crossing Eötvös Basin. EOT and MPT (Eocene-Oligocene and Miocene-Pliocene transitions, respectively) are age assigned to seismic reflectors based on the ODP Site 696 stratigraphy, shown in a simplified lithological log of Site 696 (modified after Barker et al., 1988). Age assessment for the 'EOT' seismic marker is from Houben et al. (2013).

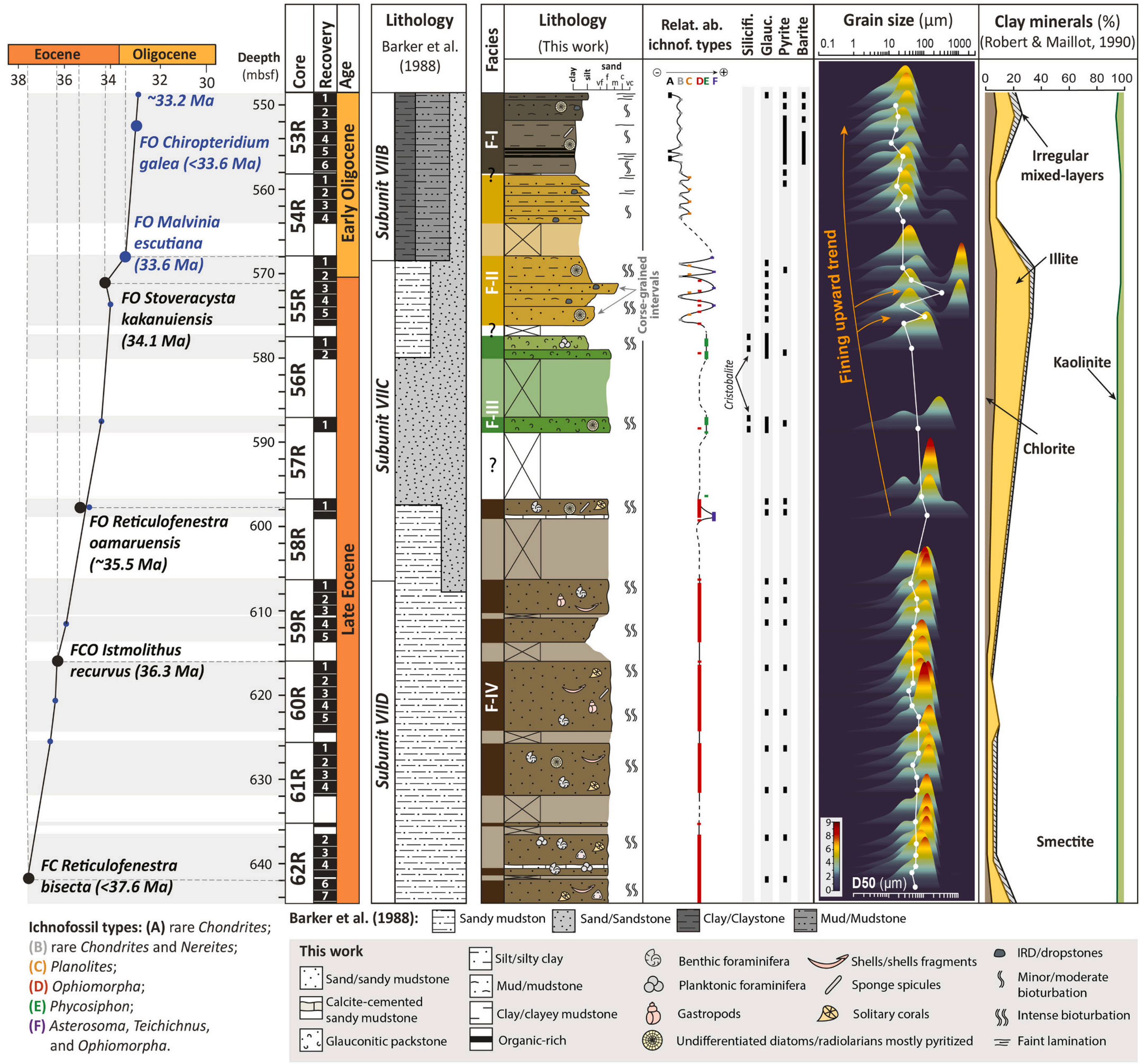

Fig. 3. Stratigraphic log of the studied sedimentary section from Hole 696B. From left to right: Age-depth plot based on biostratigraphy, cores, core recovery, lithology/facies, sediment textures, relative abundance of ichnofacies types, authigenic/diagenetic mineral occurrences, grain size, and clay minerals (%). Core recovery: black = recovery, white = no recovery. Note that divisions in the recovery denote the sections for each core, from 1 to X from top to bottom. Biostratigraphic age constraints are from Wei and Wise (1990) and Houben et al. (2013, 2019). For comparison, lithologic subunits are represented as defined on shipboard (Barker et al., 1988) together with the lithologies re-defined in this work. Grain size is represented here as down-section total grain size distribution. In this distribution plot (for each characteristic individual sample particle size distribution), the y-axis represents depth down the section, x-axis is particle size, and the colors represent the volume of the sample within those grain-size classifications, warmer colors being higher percentages, cooler colors lower percentages. Additionally, the mean grain size evolution (D50 µm) is plotted. Clay minerals are from Robert and Maillot (1990).

Paléoenvironnements Océaniques et Continentaux lab (EPOC, Bordeaux, France). A total of 41 sediment samples were dried overnight in an oven at 40 °C, sieved to remove coarse-grained (>2000 µm in diameter) particles, then measured in a laser microgranulometer Malvern mastersizer hydro 2000G with automatic sampling (0.020 to 2000 µm).

X-ray diffraction (XRD) measurements at the Instituto Andaluz de Ciencias de la Tierra (CSIC-University of Granada, Spain) were used to determine the average bulk mineralogical composition of the different facies.

3.2.2. *Elemental and stable isotope analyses*

Total organic carbon (TOC), total nitrogen (TN) and the carbon (δ^{13}C) and nitrogen (δ^{15}N) isotopic composition of bulk sediments were measured to derive a record of the biological origins of the organic matter in the sediments (i.e., the mixing trend between terrestrial and aquatic sources of organic matter) (e.g., Meyers, 1997; Muller and Voss, 1999; Huon et al., 2002).

Weight percentages of total organic carbon (% TOC) and total nitrogen (% TN) were obtained using a LECO C—S 125 analyzer at the Environnements et Paléoenvironnements Océaniques et Continentaux lab (EPOC, Bordeaux, France) through the total combustion of 70 sediment samples treated with 1 N HCL to eliminate inorganic carbon. The precision of TOC measurements based on standards and replicates was better than 0.5%, while TN measurements were better than 0.3%.

Portions of carbonate-free sediments were analyzed at the University of Bordeaux to determine δ^{13}C and δ^{15}N composition using a Carlo Erba CN analyzer 2500 interfaced directly to a Micromass-Isoprime mass spectrometer. The δ^{15}N and δ^{13}C values were determined on dried, ground bulk sediments and reported in delta notation (eqs. (1) and (2)). Sediments were encapsulated in tin and injected into a Flash 200 elemental analyzer. Each sample was first oxidized under high temperature conditions (~1040 °C) by cobalt and chrome oxides, then reduced in a second column by copper. The resulting gas (N2) was: (1) transferred to the mass spectrometer where it was ionized, (2) accelerated under high voltage (400 μA), (3) deflected after its molecular weight, and (4) caught in a collector. Moreover, δ^{15}N values from certified and in-house standards (Acetanilide, Casein, Glycine, N1 and sdk) were measured and used to adjust the δ^{15}N values from each sediment sample. The precision of the δ^{15}N analyses based on standards and replicates was better than 0.2‰. δ^{13}C ratios were obtained following the same procedure as for the δ^{15}N measurements. According to replicates and internal standards, the absolute precision of δ^{13}C is better than 0.1‰.

$$\delta^{15}N\ (‰ vs.Air) = \left(\frac{\mathrm{N}^{15}/\mathrm{N}^{14}\mathrm{Csample}}{\mathrm{N}^{15}/\mathrm{N}^{14}\mathrm{standard}} - 1\right) \mathrm{x}\ 10^{3} \tag{1}$$

in which atmospheric N2 is the reference standard (with a δ^{15}N = 0‰)

$$\left(\delta^{13}C\ (‰ vs.Air) = \left(\frac{C^{13}/C^{12}Csample}{C^{13}/C^{12}standard} - 1\right) x\ 10^{3}\right. \tag{2}$$

in which Vienna PeeDee Belemnite (VPDB) is the reference standard (with a δ^{13}C = 0‰).

In order to identify the primary factors influencing variations in the elemental and stable isotope analysis, we conducted a Principal Component Analysis (PCA), the simplest multivariate analysis involving a mathematical procedure that transforms a number of possibly correlated variables into a smaller number of groups of closely related variables (e.g., Jolliffe, 2002). PCA computations were performed using the PAST free software package version 2.10 (Hammer et al., 2001).

3.2.3. Lipid biomarker (n-alkane) analyses

Long-chain normal *n*-alkanes (C_{23}-C_{31}) provide details about the production, delivery, and preservation of organic matter in sediments, and their distribution can be used to discriminate between terrigenous and marine organic matter, thus providing insight into paleovegetation and paleoclimates (e.g., Meyers, 1997; Ficken et al., 2000; Schefuß et al., 2003; Vogts et al., 2009; Duncan et al., 2019).

The *n*-alkane analyses were performed at the Laboratoire d'Océanographie et du Climat, Expérimentations et Approches Numériques (LOCEAN-Université Pierre et Marie Curie, Paris, France). First, 70 sediment samples were freeze-dried and crushed to a fine powder. Total lipids were extracted from ~9.5 to 15 g of homogenized sediment using a solvent mixture of 40 mL CH2Cl2/CH3OH (3:1, *v*/*v*) to which an internal standard (5 α-cholestane) was added. The *n*-alkane fraction was separated from the polar lipids over a silica column using 3 mL hexane as eluent. After drying the fraction, elemental sulfur was removed through the TBA (tetrabutylammonium) sulfite method (Jensen et al., 1977; Riis and Babel, 1999). Samples were analyzed on a gas chromatograph (GC) (Agilent 6890 N) equipped with a flame ionization detector (FID) and fitted with a 30 m long DB5 fused silica capillary column (0,32 mm i.d., 0.25 μm film thickness). Quantification of *n*-alkanes was performed manually, by peak area integration in FID chromatograms relative to the internal standard, following eq. (3). The GC oven temperature program was set at 120 °C at a rate of 30 °C/min, then raised to 320 °C at a rate of 5 °C/min.

$$[\mathrm{CnH2n}+2](\mathrm{ng/g}) = \frac{\mathrm{Area\ ChH2n} + 2\ \mathrm{x\ standard\ concentration\ (ng/g)}}{\mathrm{Injected\ vol}/(\mathrm{Area\ standard\ x\ sample\ weight\ (g)\ )}} \tag{3}$$

Contribution of *n*-alkane in sediments from different biological sources (vascular land plants, marine algae or petroleum origin) can be assessed on the basis of specific carbon chain length variations (e.g., Cranwell, 1973; Rieley et al., 1991; Bi et al., 2005). The following *n*-alkane-based indices were used in this study:

1. Carbon Preference Index (CPI) (Farrington and Tripp, 1977; Kennicutt et al., 1987; Rieley et al., 1991; Hedges and Prahl, 1993; Bush and McInerney, 2013):

$$\mathrm{CPI} = \frac{1}{2}\left(\left(\frac{\Sigma\mathrm{odd}\ (n-\mathrm{C25}-31)}{\Sigma\mathrm{even}\ (n-\mathrm{C24}-30)}\right) + \left(\frac{\Sigma\mathrm{odd}\ (n-\mathrm{C25}-31)}{\Sigma\mathrm{even}\ (n-\mathrm{C26}-30)}\right)\right)$$

2. Average chain length (ACL) (Poynter et al., 1989; Simoneit et al., 1991; Ficken et al., 2000; Schefuß et al., 2003):

$$\mathrm{ACL} = \frac{\Sigma[\mathrm{Ci}]\cdot i}{\Sigma[\mathrm{Ci}]}$$

C*i* = carbon number of the odd chain length *n*-alkanes (i.e., from *n*-C_{25} to *n*-C_{31}).
i = concentration of the odd *n*-alkanes.

3. Terrestrial *n*-alkanes Index (TI) (De Mahiques et al., 2017):

$$\mathrm{TI} = \frac{\Sigma\mathrm{C27}+29+31}{\mathrm{TOC}}$$

4. Aquatic plant *n*-alkane proxy (P_{aq}) (Ficken et al., 2000):

$$\mathrm{P}aq = \frac{\mathrm{C23}+\mathrm{C25}}{\mathrm{C23}+\mathrm{C25}+\mathrm{C29}+\mathrm{C31}}$$

Relationships between *n*-alkane indices were investigated using Pearson's correlation coefficients, considered statistically significant at $p < 0.05$.

3.2.4. Palynological data

Terrestrial palynomorph identification in a total of eight samples collected between 645.6 and 597.2 mbsf spanning the late Eocene (~37.6–35.5 Ma; Fig. 3) served to compliment sedimentological interpretations. Fossil spores/pollen grains were identified microscopically using Leica DM500 and Leica DM2000 transmitted light microscopes at 200× and 1000× magnification at the Department of Geography and Environmental Sciences (University of Northumbria, England). In addition, we compare our new results to palynological investigations on the same sedimentary record (late Eocene-early Oligocene, ~37.6–32.2 Ma; Houben et al., 2013, 2019), in view of the abundance of terrestrial palynomorphs relative to the abundance of marine dinocysts, a commonly used proxy to trace organic matter sourcing.

4. Results

4.1. Sediment facies in Hole 696B

Four lithofacies could be defined, numbered F-I through F-IV, from top to bottom (in contrast with the three subunits by Barker et al., 1988) (Fig. 3).

4.1.1. *Facies I – claystone and clayey mudstone*

Facies I extends from 558 to ~550 mbsf (cores 53R sections 1 to 7). This facies consists of massive very dark gray to dark brown claystones and gray clayey mudstones (Figs. 3 and 4A). Black carbonaceous-rich mudstone bands up to 1.5 cm thick were observed interbedded throughout core 53R section 5 (556.4 to 554.9 mbsf) (Fig. 4B).

Facies I is scarcely to moderately bioturbated, containing sparse laminations. Local occurrences of ichnofossils mainly consist of *Chondrites*, probable *Nereites* and rare *Planolites* (Figs. 4A and B). Rare millimeter-sized ice rafted debris (IRD) was observed in core 53R sections 1 and 2 (Fig. 3). The claystone matrix consists of clay-size particles and clay minerals, dominated by smectite (Fig. 5A). Quartz, feldspar, rare diatom tests and indistinct, pyritized siliceous bioclast fragments, as well as pyrite and barite, are present in the clay fraction (e.g., Fig. 5B, C; *Supplementary Fig. S1A-C*). Organic matter relicts were observed in the black carbonaceous-rich mudstone bands, as shown by ESEM analysis including EDX spectra (Fig. 5C, D).

4.1.2. *Facies II – silty to sandy mudstone*

Facies II extends from 575.9 to 558.5 mbsf (core 55R sections 1 through 6 and 54R sections 1 through 4), while no sediments were recovered from 568.2 to 563 mbsf (Fig. 3). This facies consists of massive and mottled light olive gray and pale yellow silty mudstones (Figs. 3 and 4C-E). Sandy mudstones are interbedded throughout core sections 55R-5 and 55R-3, forming two coarse-grained intervals that consist mainly of sub- to well-rounded quartz and rock fragments (Fig. 5E, F). Quartz grains are marked by conchoidal fracture surfaces (Fig. 5F). Reworked glaucony grains were also identified. Sediments within these two coarse-grained intervals show coarsening-upward sequences.

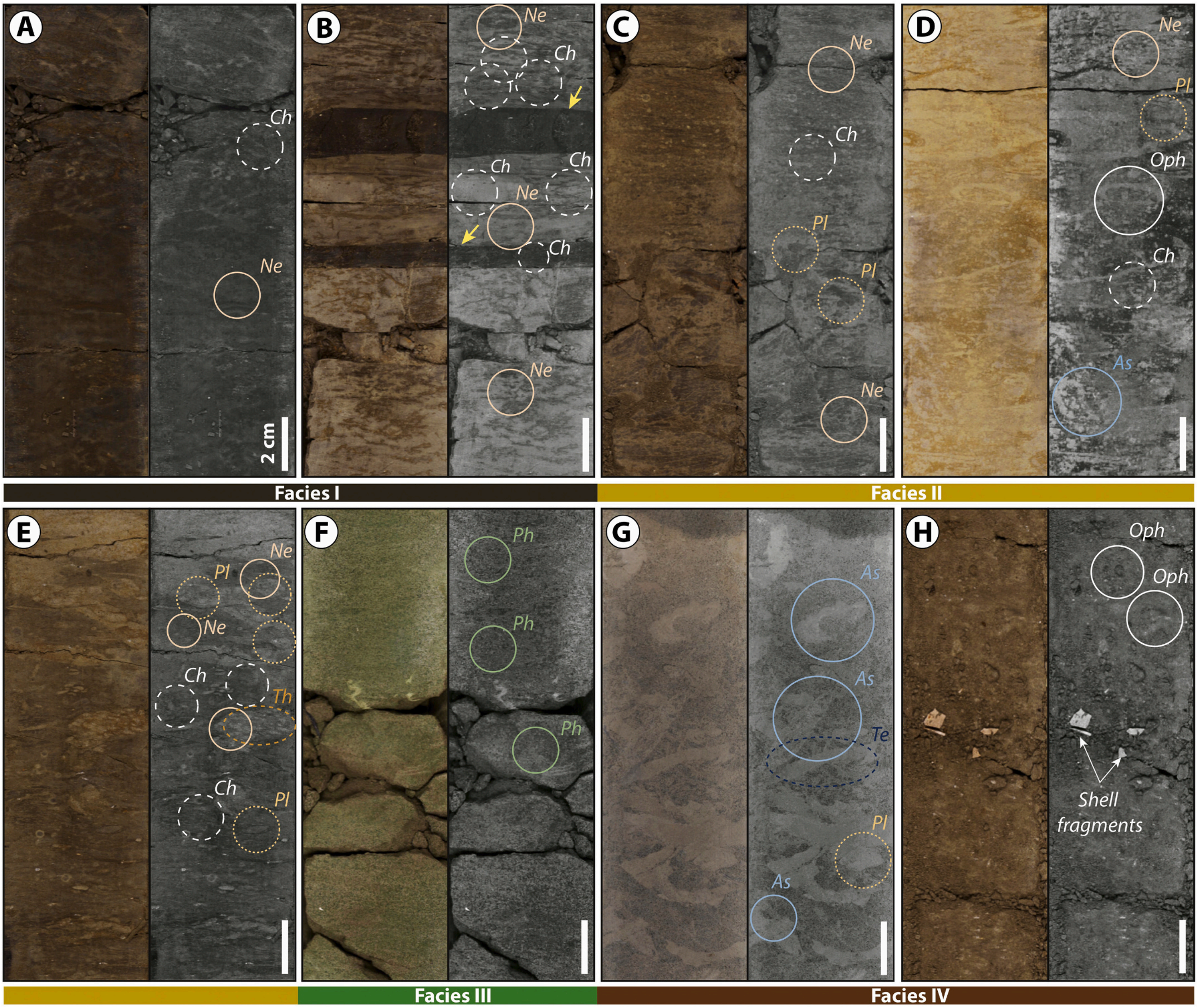

Fig. 4. Detailed sediment facies and associated ichnofabrics identified at Hole 696B. A) and B) Core slab examples of Facies I (claystone and clayey mudstone; core sections 53R-5) showing *Chondrites* (Ch) and *Nereites* (Ne) burrows. C), D) and E) Core slab examples of Facies II (sandy to silty mudstone; core 54R section 3 and 55R sections 1 and 4, respectively) displaying burrows of *Chondrites* (Ch), *Nereites* (Ne), *Planolites* (Pl), *Ophiomorpha* (Oph), *Asterosoma* (As) and *Thalassinoides* (Th). F) Core slab example of Facies III (glauconitic packstone; core section 56R-2) with possible *Phycosiphon* (Ph) burrows. G) and H) Core slab examples of Facies IV (carbonate-cemented [G] and structureless [H] sandy mudstone; core 58R section 2 and 59R section 1, respectively) displaying burrows of *Asterosoma*, *Planolites*, *Ophiomorpha* and *Teichichnus* (Te). Shell fragments are also shown in (H). The vertical white bar scale is 2 cm.

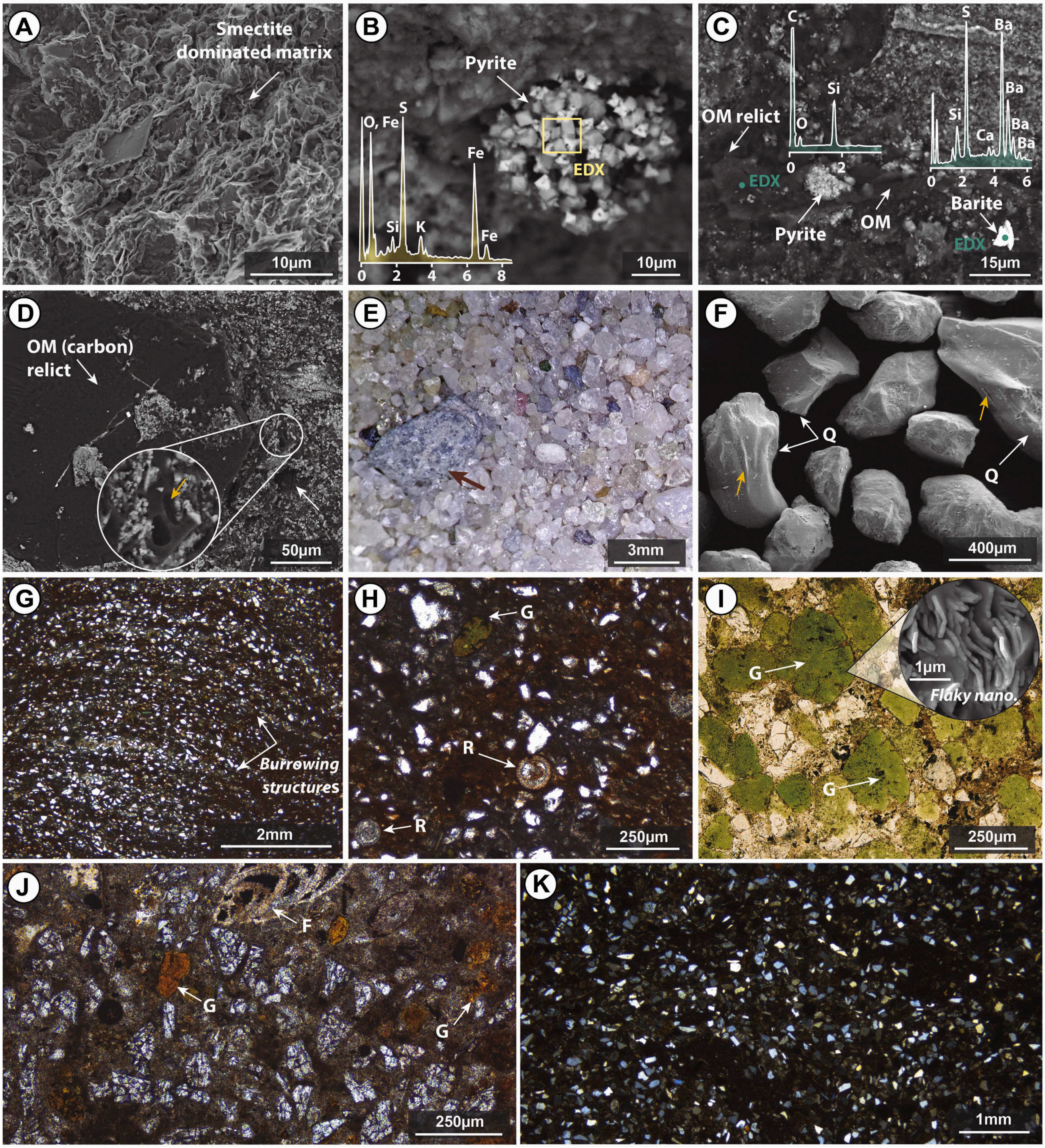

Fig. 5. Sedimentation at the studied Hole 696B sedimentary section. A) SEM photomicrograph (SE) of Facies I (core sections 53R-4) showing a smectite-dominated matrix. B) SEM (SE) photomicrograph and related energy-dispersive X-ray (EDX) analysis of Facies I (core section 53R-5) framboidal pyrite. C) SEM (SE) photomicrograph showing examples of organic matter (OM) relicts, barite and framboidal pyrite in Facies I (core section 53R-5, black organic rich-layer). EDX analysis of the OM relict (see C peak in the spectrum) and barite (see the triple Ba peaks in the spectrum) are also shown. D) SEM (SE) photomicrograph of a detailed OM (carbon) relict within Facies I (core section 53R-5, black organic rich-layer). Note also bioclast remains (yellow arrow). E) and F) Sieved siliciclastic grains (binocular glass and SEM (SE) photomicrographs, respectively) corresponding to one of the coarse-grained mudstone intervals observed within Facies II (core section 55R-3). Quartz and alkali feldspars grains dominate the siliciclastic components. The red arrow in (E) is points to a possible magmatic rock fragment, whereas yellow arrows in (F) indicate quartz grains with conchoidal fracture surfaces. G) Plane-polarized light (PPL) photomicrograph showing burrowed silty mudstone of Facies II (core section 55–4). H) PPL photomicrograph of Facies II (core section 55R-4). G: detrital glaucony grain; R: radiolarian tests. I) PPL photomicrograph of Facies III (glaucony-rich packstone sediments; core section 56R-2). Enlarged area corresponds to a SEM (SE) photomicrograph displaying a flaky honeycombed and lamellar glaucony nanostructure. J) PPL photomicrograph of Facies IV (core section 62R-4) showing predominantly angular to subangular grains of quartz and alkali feldspars. G: poorly evolved glaucony grains; F: benthic foraminifer. K) Cross-polarized light (CPL) photomicrograph of Facies IV (core section 58R-2) showing subangular to well-rounded siliciclastic components: quartz, alkali feldspar, plagioclase and mica grains. (For interpretation of the references to colour in this figure legend, the reader is referred to the web version of this article.)

No primary sedimentary structures were observed due to ubiquitous moderate to intense bioturbation. The ichnoassemblage is relatively diverse, mainly consisting of *Planolites*, *Chondrites* and *Nereites*. Furthermore, traces of *Thalassinoides*, *Ophiomorpha* and *Asterosoma* are locally observed in core 55R sections 3 to 5 (Fig. 4C-E). Burrows are filled with silt and fine sand (e.g., Fig. 5G). Common millimeter-sized IRD was also observed (see Fig. 3). Alkali feldspar, glaucony fragments and mostly pyritized radiolarian tests (and probably diatoms) were also identified (Fig. 5H).

4.1.3. Facies III – glauconitic packstone

Facies III extends from ~588.8 to 577.9 mbsf (core 57R section 1 to 56R section 1; Fig. 3); no sediments were recovered from 580.5 to 587.6 mbsf. Facies III (very poorly recovered) includes greenish gray glauconitic packstone and pale yellow to light olive gray silty and sandy mudstone with abundant glaucony grains (López-Quirós et al., 2019) (Fig. 4F).

According to López-Quirós et al. (2019), mature glauconitized grains of 125–500 µm within the glauconitic packstone facies form by authigenic transformation of pellets in sandy to silty smectite-rich, mixed terrigenous-carbonatic sediments (Fig. 5I and *Supplementary Fig. S1E*). Other authigenic minerals such as zeolite, pyrite and silica are found in the matrix among glaucony grains. Quartz, alkali feldspar and clay minerals are present in the clay fraction (see e.g., Fig. 3 and Supplementary Fig. S5 in López-Quirós et al., 2019). This facies is moderately bioturbated, with *Phycosiphon* exclusively (e.g., Fig. 4F).

4.1.4. Facies IV – Sandy mudstone

Facies IV extends from the bottom of the hole at 645.6 to ~597.2 mbsf (core 62R section 8 to 58R section 1; Fig. 3). Facies IV consists of pale olive to olive gray sandy mudstone. Minor lithologies include glaucony-bearing, carbonate-cemented sandy mudstone (Fig. 4G) and clayey mudstone.

Sediments are structureless, and contain abundant millimeter-size bivalve and probably gastropod shell fragments (Fig. 4H). Terrigenous components are mainly angular to subangular grains of predominantly quartz with subordinate alkali feldspar, mica and undifferentiated rock fragments (Fig. 5J, K), although moderate occurrences of well-rounded grains were observed in core 59R. Benthic foraminifera are very abundant and diverse in the lower part of Facies IV (cores 61R, 62R) (Figs. 3 and 6A), decreasing in abundance above 626 mbsf (cores 59R, 60R). Overall, benthic foraminifera are moderate to well-preserved (Fig. 6A). Sediments of this facies are barren of planktonic foraminifera, with the exception of a carbonate-cemented sandy mudstone at 640 mbsf (core section 62R-4; Fig. 6B) with moderately abundant but low-diversity planktonic assemblage. Phytoplankton *Bolboforma* were recognized in cores 62R-60R (Fig. 6B). The pollen and spore assemblage contains the paratropical taxa *Arecipites* (Arecaceae), *Beaupreaidites* (Beauprea), *Myrtaceidites* (Myrtaceae) and *Dacrydiumites* (*Dacrydium*), in addition to the typical *Nothofagus* (pollen taxa: *Nothofagidites*) podocarp conifer assemblage (Fig. 6C). In addition, Barker et al. (1988) reported rare reworked freshwater diatoms in core 58R-CC. Silt-sized orange to brownish-green immature (nascent or slightly evolved) glaucony grains were observed throughout (Fig. 5J), but more abundant at some levels: 641–639, 632–630, and 608–597.2 mbsf (Fig. 3). The bioturbation is moderate to intense, with well-preserved traces of pellet-lined *Ophiomorpha* throughout (e.g., Fig. 4H). Well-preserved *Asterosoma* and *Teichichnus* ichnofossils were observed in the carbonate-cemented sandy mudstone at ~599 mbsf (Fig. 4G).

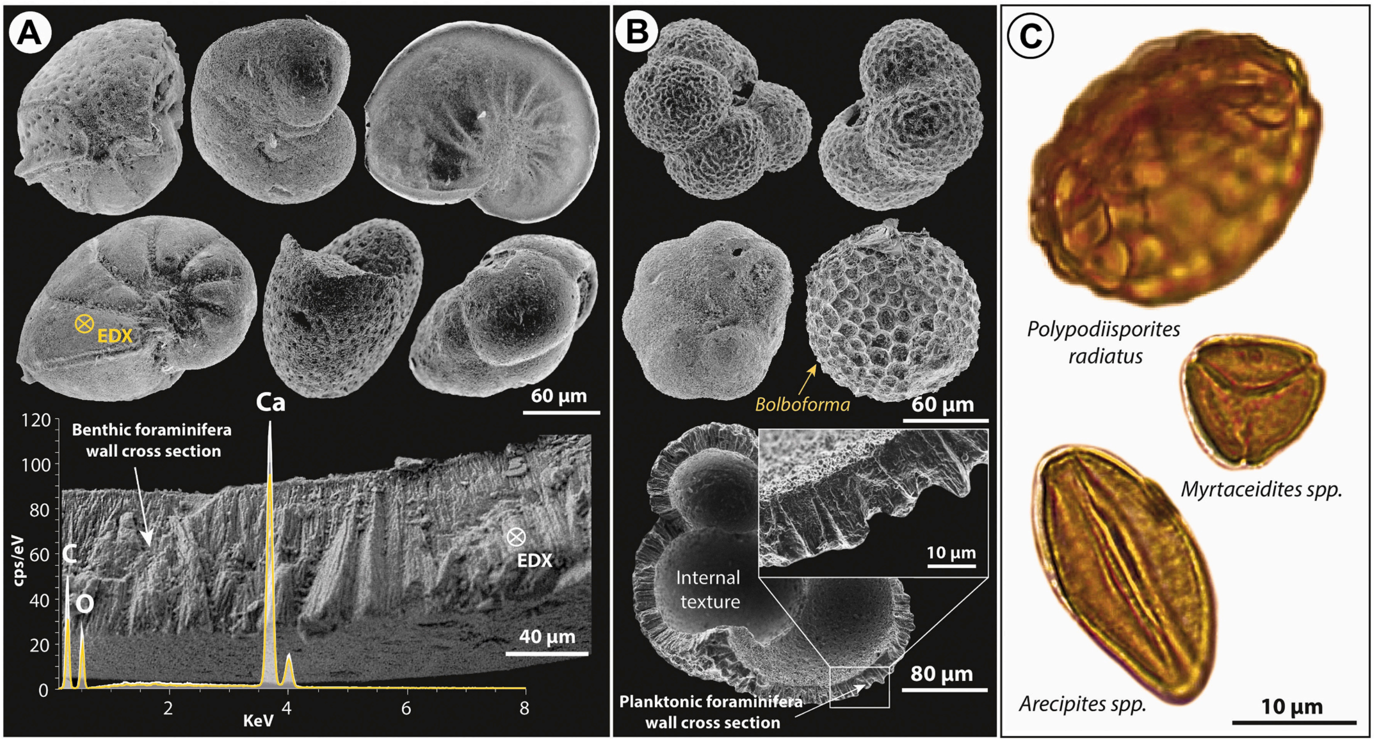

Fig. 6. A) SEM (SE) photomicrographs of moderate to well-preserved benthic foraminifera whole tests in Facies IV (cores 62R-60R). A detailed cross-sectional view of the wall of a benthic foraminifera test is also shown. Note that corresponding surface EDX analysis of benthic foraminifera indicate a calcium carbonate composition. B) SEM (SE) photomicrographs of moderate- to well-preserved planktonic foraminifera (white arrow) and *Bolboforma* (yellow arrow) in Facies IV (core section 62R-4). A detailed artificially broken planktonic foraminiferal test (to reveal internal texture) is also shown. Enlarged area corresponds to the cross-sectional view of the wall texture, displaying moderate to good preservation. C) Selected fossil spore/pollen grains of Facies IV. (For interpretation of the references to colour in this figure legend, the reader is referred to the web version of this article.)

4.2. Vertical distributions of TOC, TN, C/N ratio, δ^{13}C and δ^{15}N

The vertical distributions of TOC and TN display a progressive increase from the late Eocene to the early Oligocene (Fig. 7). Highest TOC and TN concentrations were found in Facies I (Table 1; Fig. 7), the highest one detected at 556 mbsf in a black carbonaceous-rich mudstone band within core section 53R-5 (TOC: 1.25% and TN: 0.09%; see *Supplementary Fig. S1A*). Facies II, III and IV display progressively lower TOC and TN concentrations (Table 1; Fig. 7).

The vertical distribution of C/N exhibits small variations with the exception of a large peak (18%; Table 1) in the carbonate-cemented sandy mudstone horizon at ~599 mbsf (core section 58R-2; Facies IV) (Fig. 7), as shown for each facies (from I to IV) in Table 1 (*Supplementary Table S1*). The vertical distribution of δ^{13}C varies from −25.60 to −23.95‰, whereas δ^{15}N varies from 1.34 to 3.49 (Fig. 7; Table 1). The highest δ^{15}N values were found in Facies III and IV (Table 1), in the glauconitic packstone at ~580 mbsf (core section 56R-2; Facies III). In contrast, δ^{15}N values could not be determined because of low N concentration in the carbonate-cemented sandy mudstone horizon at ~599 mbsf (core section 58R-2) (Table 1; *Supplementary Table S2*). For the δ^{13}C and δ^{15}N range and average values in each facies (from I to IV) see Table 1 (for complete information see *Supplementary Table S1*).

The result of PCA revealed two main axes that explain most variation in geochemical parameters (TOC, TN, C/N, δ^{13}C and δ^{15}N) (see *Supplementary Fig. S2*). The first principal component (PC1) accounted for 82.3% of the variation; together with the second principal component (PC2), this value increased to 91%. The correlation between TOC, C/N and δ^{13}C with PC1 is high, but correlation with TN and δ^{15}N is low. In contrast, the correlation of TN and δ^{15}N with PC2 is moderate, whereas the TOC, C/N and δ^{13}C exhibited low values. The PCA biplot mainly revealed a deviation of the δ^{15}N and C/N ratio with respect to the rest of the components.

4.3. Distribution of *n*-alkane variables

Total concentrations of C_{23}-C_{31} *n*-alkanes range from 236 ng/gTOC to 1639 ng/gTOC in Facies I, with an average value of 953.8 ng/gTOC (Fig. 8; *Supplementary Table S2*). Long chain *n*-alkanes n-C_{27}, n-C_{29} and n-C_{31} are the most common (*Supplementary Table S2* and *Fig. S3*), n-C_{29} being the most prominent. However, n-C_{27} and n-C_{29} are the dominant *n*-alkanes in the interbedded black carbonaceous-rich mudstone bands, which also have increased proportions of n-C_{23} and n-C_{25} (Fig. 8; *Supplementary Table S2* and Fig. S3). The average values of CPI, ACL, P*aq*, TI, n-C_{29}/n-C_{27}, n-C_{27}/n-C_{31} and n-C_{23}/n-C_{29} are shown in Table 1 (*Supplementary Table S2*). The highest P*aq* and lowest TI concentrations occur in the interbedded black carbonaceous-rich mudstone bands (Fig. 8; *Supplementary Table S2*).

Total concentrations of C_{23}-C_{31} *n*-alkanes range from 424 to 1523 ng/gTOC, averaging 687 ng/gTOC in Facies II (Fig. 8; *Supplementary Table S2*). Long chain *n*-alkanes such as n-C_{27}, n-C_{29} and n-C_{31} dominate, with n-C_{29} most prominent (see *Supplementary Fig. S3*). The average values of CPI, ACL, P*aq*, TI, n-C_{29}/n-C_{27}, n-C_{27}/n-C_{31} and n-C_{23}/n-C_{29} are shown in Table 1 (for details, see *Supplementary Table S2*). TI exhibits the highest values in the studied section (Table 1).

Total concentrations of C_{23}-C_{31} *n*-alkanes range from 468 ng/gTOC to 742 ng/gTOC, averaging 592.7 ng/gTOC in Facies III (Fig. 8; *Supplementary Table S2*). Although n-C_{25}, n-C_{27}, n-C_{29} and n-C_{31} are abundant, n-C_{29} is the most prominent (*Supplementary Fig. S3*). The average values of ACL, P*aq* and the n-C_{29}/n-C_{27}, n-C_{27}/n-C_{31} and n-C_{23}/n-C_{29} display slight variability, with higher variability in CPI and TI (Table 1; Fig. 8). CPI exhibits the highest values in the studied section (Table 1).

Total concentrations of C_{23}-C_{31} *n*-alkanes average 487 ng/gTOC in Facies IV (Fig. 8; *Supplementary Table S2*). The *n*-alkane distributions display prominent peaks in n-C_{23}, n-C_{25}, n-C_{27}, n-C_{29} and n-C_{31} (*Supplementary Fig. S3*). Mid-chain *n*-alkanes (i.e., n-C_{23} and n-C_{25}) show slightly lower concentrations than long chain homologs (> n-C_{27}).

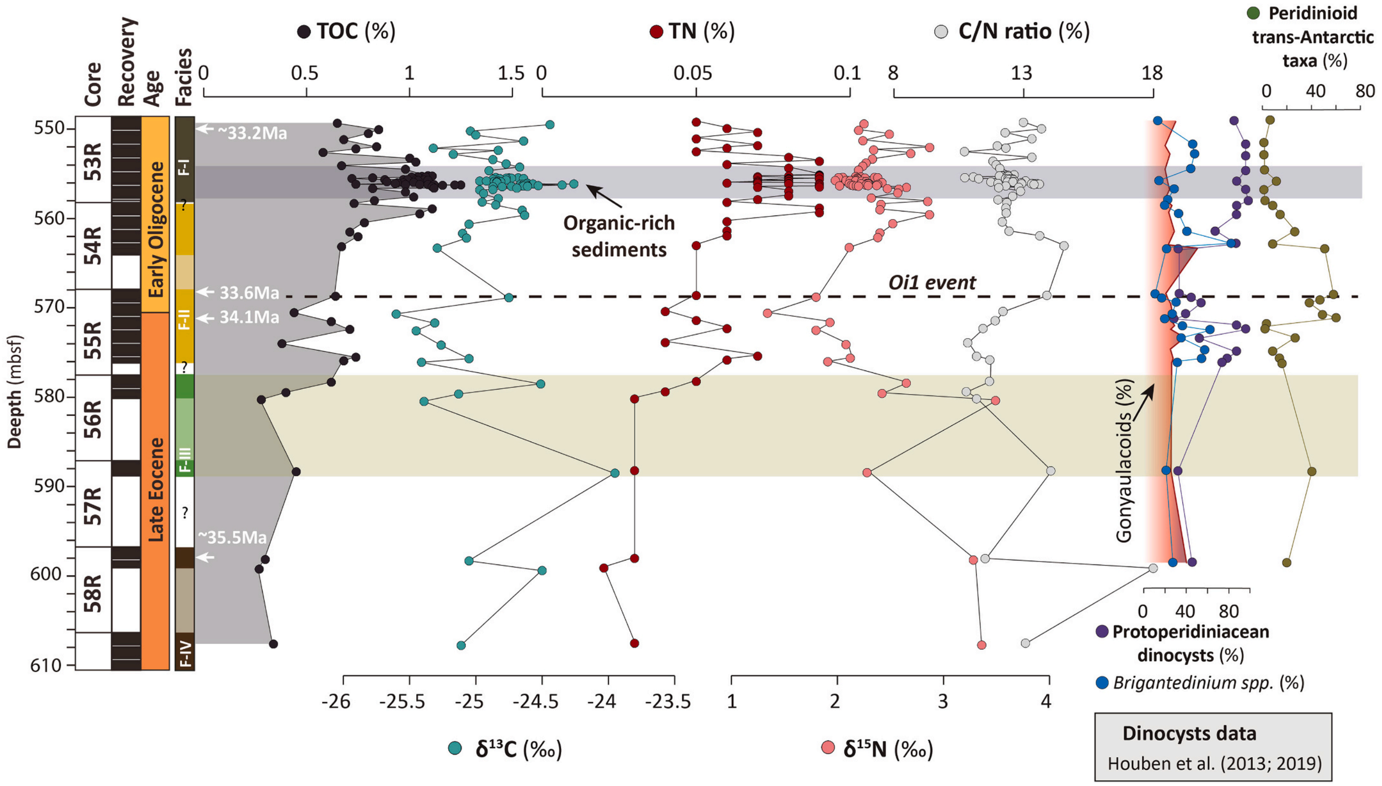

Fig. 7. Vertical down section distribution of total organic carbon (TOC), total nitrogen (TN), C/N, δ^{13}C and δ^{15}N values for studied Hole 696B sediment section, versus age. Gray shading: organic rich core 53R section 5 within Facies I; Green shading: glauconitic Facies III. Dinocyst assemblages are from Houben et al. (2013, 2019). (For interpretation of the references to colour in this figure legend, the reader is referred to the web version of this article.)

Table 1
Average values of the bulk organic matter (TOC, TN, related C/N ratio, δ^{13}C and δ^{15}N) and molecular (*n*-alkane) variables. Min-max values in parenthesis. For complete information see *Supplementary Tables S1* and *S2*. Note that average values in Facies IV are distinguished between background sedimentation (BS) and carbonate-cemented (CC).

Variables	Facies I	Facies II	Facies III	Facies IV
Bulk organic matter (elemental and stable isotope) variables				
TOC (%)	0.96 (0.58 to 1.25)	0.65 (0.38 to 0.78)	0.44 (0.62 to 0.28)	BS: 0.32 CC: 0.27
TN (%)	0.08 (0.05 to 0.09)	0.05 (0.04 to 0.07)	0.04 (0.05 to 0.03)	BS: 0.08 CC: 0.02
C/N ratio (%)	12.48 (10.74 to 13.71)	12.38 (10.86 to 14.57)	11.94 (10.81 to 14.06)	BS: 12.31 CC: 18
δ^{13}C (‰)	−24.77 (−25.32 to −24.26)	−25.21 (−25.60 to −24.75)	−24.75 (−25.39 to −23.95)	BS: −25.08 CC: −24.50
δ^{15}N (‰)	2.31 (1.98 to 2.87)	2.02 (1.34 to 2.54)	2.71 (2.28 to 3.49)	BS: 3.32 CC: 0
Molecular (n-alkane) variables				
CPI (ng/g)	2.4 (1.6 to 3.5)	4.2 (2.5 to 5.6)	6.22 (3.23 to 11.94)	BS: 6.13 CC: 0
ACL (ng/g)	27.3 (26.5 to 28.8)	27.8 (27.1 to 28.6)	27.47 (27.30 to 27.69)	BS: 27.08 CC: 27.91
Paq (ng/g)	0.4 (0.2 to 0.6)	0.33 (0.18 to 0.48)	0.41 (0.39 to 0.44)	BS: 0.47 CC: 0.29
TI (ng/g)	468.4 (150 to 788.2)	648.5 (384.4 to 1318.4)	752.85 (661.29 to 964.29)	BS: 933 CC: 851.85
n-C$_{29}$/*n*-C$_{27}$ (ng/g)	1 (0.83 to 1.61)	1.3 (0.63 to 3.05)	1.23 (0.98 to 1.45)	BS: 1.02 CC: 1.61
n-C$_{27}$/*n*-C$_{31}$ (ng/g)	1.35 (0.76 to 2.29)	1.10 (0.32 to 2.77)	0.98 (0.77 to 1.29)	BS: 1.06 CC: 1.71
n-C$_{23}$/*n*-C$_{29}$ (ng/g)	0.75 (0.13 to 1.40)	0.44 (0.13 to 0.83)	0.63 (0.56 to 0.68)	BS: 0.94 CC: 0

Alkanes *n*-C$_{23}$, *n*-C$_{24}$, *n*-C$_{26}$, *n*-C$_{28}$ and *n*-C$_{30}$ were below detection at ~599 mbsf (core section 58R-2) (Table 1; *Supplementary Table S2*). The average values of CPI, ACL, TI, P*aq*, *n*-C$_{29}$/*n*-C$_{27}$, C$_{27}$/*n*-C$_{31}$ and *n*-C$_{23}$/*n*-C$_{29}$ are indicated in Table 1.

Pearson's correlation coefficients were estimated between the *n*-alkane variables (*Supplementary Fig. S4*). Significant statistical correlations are found between ACL and P*aq* ($r = 0.989, p < 0.0000$), ACL and *n*-C$_{23}$/*n*-C$_{29}$ ($r = 0.964, p < 0.0000$), and P*aq* and *n*-C$_{23}$/*n*-C$_{29}$ ($r = 0.965$, $p < 0.0000$), with weaker correlations between ACL and *n*-C$_{27}$/*n*-C$_{29}$ ($r = 0.720$, $p < 0.0000$) and TI and *n*-C$_{23}$/*n*-C$_{29}$ ($r = 0.616$, $p < 0.0000$).

5. Interpretations and discussion

5.1. Evolution of depositional environments: Evidence of a sustained relative sea-level rise

The succession of sedimentary facies documents a long-term trend driven by tectonic and climatic processes, and several depositional phases can be distinguished.

5.1.1. Late Eocene (~37.6–35.5 Ma)

This interval is characterized by the sandy mudstones of Facies IV (Fig. 3), deposited with an average sedimentation rate of ~4 cm/kyr when the SOM was attached to, or quite close to, the Antarctic Peninsula. The SOM, Seymour Island and James Ross Basin constitute the remnants of an ancient back-arc basin at the northern Antarctic Peninsula (Elliot, 1988; Fig. 1B). Poorly consolidated and bioturbated sands and silts from the nearby Seymour Island and James Ross Basin reflect shallow-marine and coastal environments (e.g., Stilwell and Zinsmeister, 1992; Marenssi et al., 1998, 2002; Wellner et al., 2011) (Fig. 1B). The similar paleogeographic setting and sediment composition in Facies IV and Seymour Island could point to related sediment sources and depositional environments. However, evidence of long-distance sediment transport and reworking —e.g. well-rounded terrigenous grains, significant taphonomic features or occurrence of relict foraminifera tests— is not found (Figs. 5J, K and 6A, B). In addition, previous interpretations proposed that long-distance transport from the Weddell Sea hinterland and the Dronning Maud land via large icebergs could be a viable mechanism for the accumulation of the sand-sized fractions within Facies IV (Carter et al., 2017), despite indications of temperate depositional conditions at the SOM (Wei and Wise, 1990; Mohr, 1990, 2001; Robert and Maillot, 1990; Houben et al., 2013, 2019).

In contrast, occurrences of angular to subangular terrigenous particles (Fig. 5J) and the moderate to well-preserved in situ foraminiferal assemblages in Facies IV support intrabasinal deposition in a shallow-water (20–100 m) environment with low oxygen and salinity (Barker et al., 1988; Fig. 6A). Moderate occurrences of well-rounded terrigenous grains and reduced abundance/preservation of benthic foraminifera in core 59R-2, together with reported rare reworked freshwater diatoms in core 58R-CC (Barker et al., 1988), moreover suggest fluvial reworking, likely from local sources of the SOM. Further micropaleontological evidences such as the occurrence of abundant terrestrial palynomorphs (Houben et al., 2019) and the composition of ichnological assemblages with frequent *Ophiomorpha* and presence of *Teichichnus* (e.g., Fig. 4H) support the proposed interpretation. For example, in situ terrestrial palynomorphs recovered from Facies IV include the paratropical and warmth-loving taxa *Arecipites* (Arecaceae), *Myrtaceidites* (Myrtaceae), *Dacrydiumites* (Dacrydium) and *Polypodiisporites* cf. *radiatus* (Davallia) (e.g. Fig. 6C), not recorded in coeval Antarctic Peninsula assemblages. The Hole 696B paleoflora assemblage also reveals a greater diversity of angiosperm pollen, particularly *Proteacidites* (Proteaceae) (Mohr, 1990), compared to late Eocene Antarctic Peninsula paleoflora (e.g., Anderson et al., 2011; Warny and Askin 2011b; Warny et al., 2019). This higher diversity and presence of warmth-loving taxa would suggest that sediments from Hole 696B captured pollen and spores unique in character to the SOM, and that a significant proportion of detrital material was probably of local origin (e.g., exposed parts of the SOM). The record of *Ophiomorpha* and *Teichichnus* has been assigned to the proximal expression of the *Cruziana* ichnofacies, associated with proximal and shallow depositional settings (Miguez-Salas and Rodríguez-Tovar, 2019).

5.1.2. Latest Eocene (~35.5–34.1 Ma)

The glauconitic packstone of Facies III (Fig. 5I; *Supplementary Fig. S1E*) indicates that environments changed significantly in the shallow-water SOM environment. Development of mature glauconitic facies has been related to low sedimentation rates and recurrent winnowing action by bottom currents under suboxic, partially reducing conditions at the sediment-water interface (López-Quirós et al., 2019). Moderate bioturbation and simple monospecific trace fossil assemblages of *Phycosiphon* indicate poorly oxygenated conditions within the sediments, but oxygenated bottom water and a relatively high amount of benthic food (e.g., (Ekdale and Mason, 1988; Wetzel and Uchman, 2001; Rodríguez-Tovar et al., 2014; Fig. 4F).

This change in environmental conditions could be explained by a decrease in the delivery of proximal sediments (coarse terrigenous sediments) to the site, as the SOM moved away from the Antarctic Peninsula and subsided (became more distal) and/or a shallow seaway formed. With reduced terrigenous input, the benthic food flux might have occurred in patches bioturbated by *Phycosiphon* tracemakers. The decrease in sediment delivery to Hole 696B is supported by a drop in sedimentation rates of Facies III (~1.85 cm/kyr) by almost half as compared to that of Facies IV (~4 cm/kyr). Continuous subsidence of the SOM may have caused a relative sea-level rise and sediment-starved conditions, leading to a transgressive condensed section, with increased abundance of evolved glaucony close to the maximum flooding surface (López-Quirós et al., 2019), as documented in different glaucony-

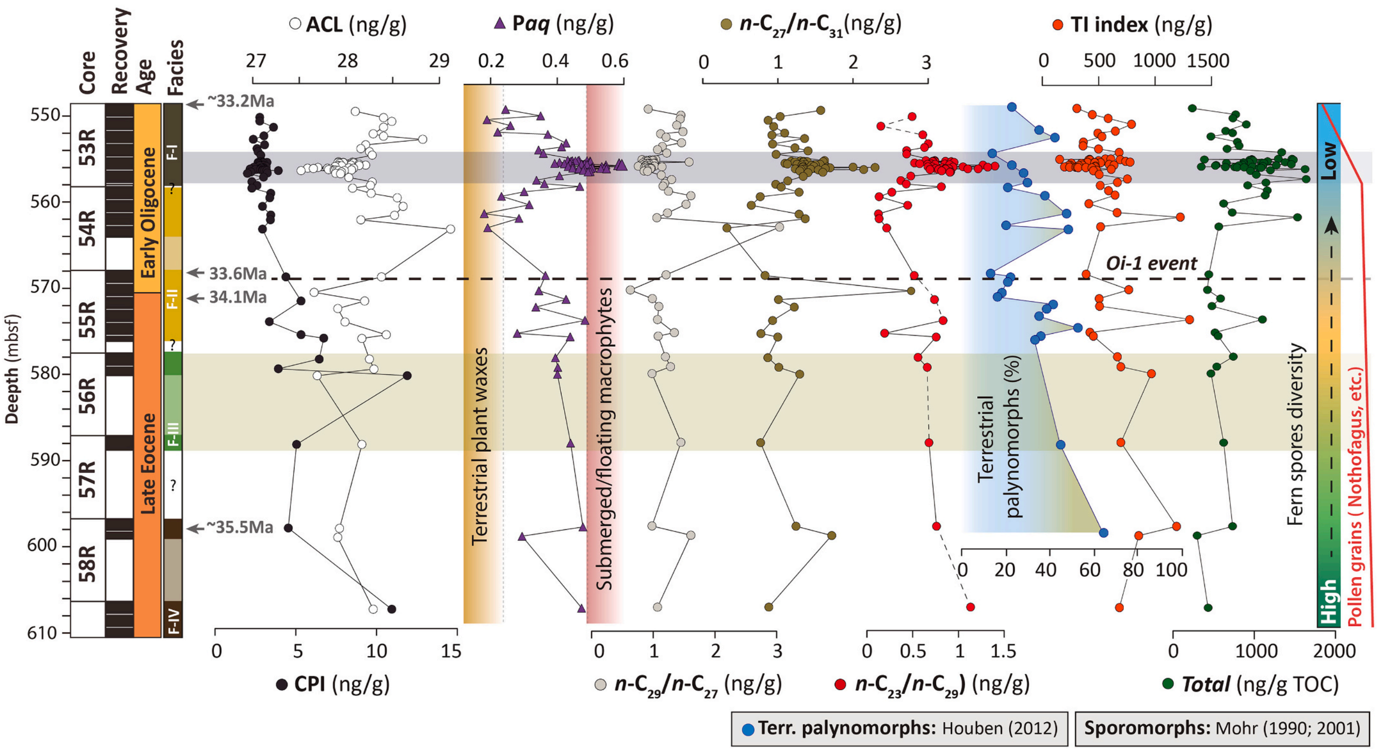

Fig. 8. Vertical distribution of *n*-alkane variables/ratios (ACL, CPI, *Paq*, *n*-C_{29}/*n*-C_{27}, *n*-C_{27}/*n*-C_{31}, *n*-C_{23}/*n*-C_{29}, TI and total concentrations of C_{23}-C_{31}) at Hole 696B sediment section versus age. Gray shading: organic rich core 53R section 5 within Facies I; Green shading: glauconitic Facies III. Terrestrial palynomorphs (undifferentiated) are from Houben (2012). Sporomorph (fern spores and pollen grains) diversity is from Mohr (1990, 2001). ACL: average chain length; CPI: carbon preference index; *Paq*: aquatic plant *n*-alkane proxy; TI: terrestrial *n*-alkane index. (For interpretation of the references to colour in this figure legend, the reader is referred to the web version of this article.)

bearing deposits (e.g., Amorosi, 1995, 1997, 2012; Giresse and Wiewiora, 2001; Chattoraj et al., 2009; Chattoraj, 2016; Banerjee et al., 2012, 2016). We propose that terrigenous input to Hole 696B started to decline ~35.5 Ma, related to the opening of the proto-Powell Basin. Several studies argue for strengthening of the circulation in the Scotia Sea and the northern Weddell Sea at this time, likely caused by opening of a shallow Drake Passage (e.g., Lawver and Gahagan, 1998; Eagles and Livermore, 2002; Livermore et al., 2007).

5.1.3. *EOT (~34.1–33.6 Ma)*

The deposition of moderately/intensely bioturbated silty mudstone of Facies II suggests favorable paleoenvironmental conditions for tracemakers at the sediment-water interphase (Fig. 4C-E). The record of *Thalassinoides* and the near absence of *Ophiomorpha*, together with the deposition of fine-grained sediments and the cohesive substrates, would indicate deposition at more distal and deeper environments (Rodríguez-Tovar et al., 2008, 2017) while SOM continued to deepen. However, two coarse-grained, coarsening upwards mudstone intervals indicate substrates favoring *Ophiomorpha*, and suggest that the deepening trend was reversed twice (Figs. 3, 5E-F). These intervals contain altered glaucony grains indicative of mechanical breakdown during transport, most likely from shallower SOM areas (López-Quirós et al., 2019). Sediment transport to the site is also evidenced by reworked dinocysts, and possibly sporomorphs (Houben et al., 2013), and conchoidal surfaces in quartz grains (Fig. 5F). The sediments may be derived from SOM coastal/shelf areas.

Intervals indicative of sea-level lowering occur during the EOT, with the oldest evidence for IRD in Facies II, showing continental ice transport to coastal/shelf areas. We thus suggest that the two coarsening-upward intervals could be related to global regressive phases due to ice sheet build-up on Antarctica, rather than the local to regional sea-level rise expected to have occurred close to the Antarctic coast, because of the combined effects of Glacial Isostatic Adjustment (GIA) and the gravitational pull of the ice sheet (e.g., Stocchi et al., 2013).

5.1.4. *Early Oligocene (~33.6–33.2 Ma)*

Sediments of Facies I document a further deepening to a deep shelf margin (i.e., hundreds of meters), while scarce laminations and the dominance of clayey/muddy sediments suggest a low-energy environment. Scarce ichnofossils are tolerant to low-oxygen conditions (*Chondrites*; Fig. 4A and B), which could be interpreted as decreasing oxygenation, i.e., highly dysoxic to suboxic bottom waters (Rodríguez-Tovar et al., 2015a, 2015b, 2019, 2020). Local presence of *Nereites* indicates short-term increased oxygen conditions, although organic matter reaching the seafloor also increased (Rodríguez-Tovar et al., 2015a, 2015b).

In this facies, pyrite occurs as both framboidal aggregates and crystalline replacements of bioclasts (Fig. 5B, C; *Supplementary Fig. S1B* and *C*). In addition, there are organic matter relicts (Fig. 5C, D), the highest TOC observed at the site (Fig. 7; *Supplementary Fig. S1A*), and barite particles resembling diagenetic barite (Paytan et al., 2002). We interpret pyrite as a *syn*-sedimentary diagenetic product formed in an environment with restricted circulation (low-oxygen). Poorly ventilated environments with near-reducing seafloor conditions reportedly promote organic matter preservation, and may lead to higher organic matter contents, where pyrite can form (e.g., Tribovillard et al., 2006). We interpret the combined observations of high TOC, pyrite and diagenetic barite as indicative of high organic productivity possibly due to upwelling, leading to low oxygen conditions at the seafloor.

5.2. Origins of the sedimentary organic matter

5.2.1. Bulk organic matter source indicators

5.2.1.1. TOC and TN values. A significant positive relationship ($R > 0.9$; Fig. 9A) between TOC and TN is observed in Hole 696B sediments. In addition, the two proxy records parallel each other throughout the studied sediment archive. TOC mostly reflects the bulk organic matter, so we assume that the TN has the same origin. C/N values (Table 1; *Supplementary Table S1*) higher than 12% (Prahl et al., 1980) or even 20% (Meyers, 1994, 1997) are considered indicative of a dominance of land-plant organic sources, whereas 4–10% would indicate marine sources (Meyers, 1994, 1997). C/N values in the study site range from 10.7% to 14%, with an average value of 12.5% (Fig. 7, Table 1), meaning the organic matter preserved in our sediments is likely to have a mixture of marine- and terrestrial-derived sources, consistent with the mixed terrestrial- and marine palynological record.

5.2.1.2. $\delta^{13}C$ and $\delta^{15}N$ values. The bulk δ^{13}C values derived from marine algae are generally in the range of −20‰ to −23‰ or even higher, whereas terrestrial derived-organic matter is characterized by relatively lower δ^{13}C values of about −27‰ (e.g., Peters et al., 1978; Meyers, 1994; Minoura et al., 1997). The δ^{13}C values at Hole 696B, ranging from −23.95‰ to −25.45‰ (average − 24.84‰; e.g., Fig. 9, Table 1), suggest contributions from both marine and terrestrial organic sources. Shipboard data on organic-carbon-rich sediments of cores 62R-53R (Barker et al., 1988; *Supplementary Fig. S5*) indicate a higher influence of marine-derived organic matter sources than of terrestrial derived material. Organic matter (kerogen) consists mainly of algal material, with the exception of two values within land-plant ranges at 622.59 and 611.04 mbsf (Espitalié et al., 1977; Tissot and Welte, 1984; *Supplementary Fig. S5*).

Marine and terrestrial origins must be taken into account when interpreting bulk δ^{15}N values. The δ^{15}N signal in deep-sea sediments primarily records the degree of fixed nitrogen (mostly nitrates, NO_3^-) utilization by phytoplankton, corresponding to the fraction of the bioavailable nitrogen supply taken up by the primary producers during photosynthesis. However, this signal can be significantly influenced by the presence of terrestrial organic matter. Typically, marine-derived organic matter exhibits δ^{15}N values from 3 to 8‰, whereas terrestrial derived-organic matter values are around +1‰ (e.g., Peters et al., 1978; Peterson et al., 1985). Notwithstanding, the primary δ^{15}N marine signature can be modified. N-fixation in warm, stratified waters discriminates very little between ^{15}N and ^{14}N, resulting in δ^{15}N values similar to atmospheric ones or lower (~0‰) (e.g., Brandes and Devol, 2002). At our study site, such hydrological conditions probably did not prevail, for which reason we exclude this process as a major cause of the δ^{15}N values from 1.34 to 3.49‰ (average 2.28‰). Water column and sedimentary denitrification processes —converting nitrates (NO_3^-) to

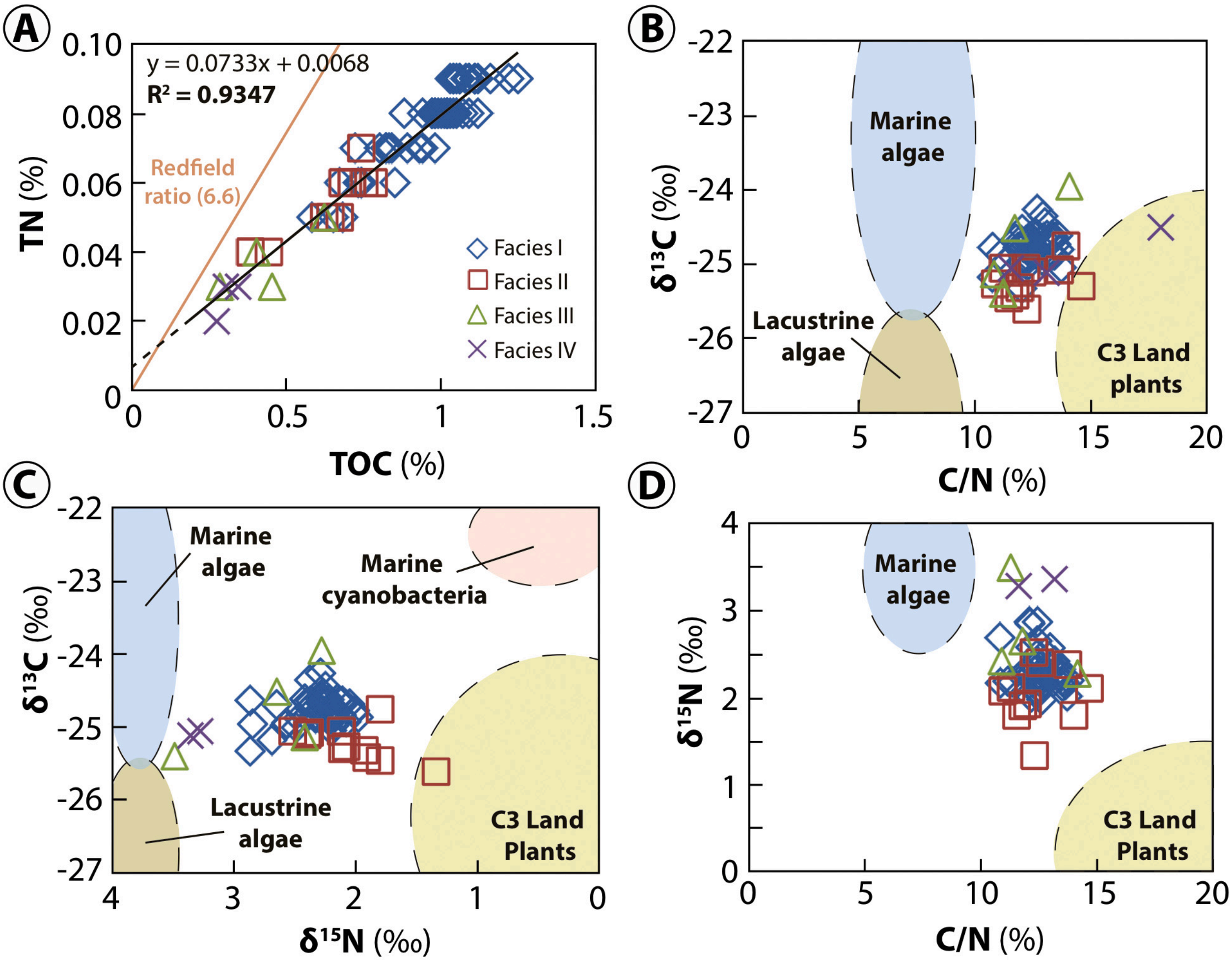

Fig. 9. A) Total nitrogen (TN) to total organic carbon (TOC) correlation. Very high correlation indicates that TN is mostly organic. The Redfield ratio of marine phytoplankton (6.6) is plotted for comparison. B), C) and D) Marine vs. terrestrial origin of the sediment organic matter as a function of δ^{13}C, δ^{15}N and C/N values. The estimated ranges of marine algae, lacustrine algae, marine cyanobacteria and C3 land plants are indicated for comparison (adapted from Meyers, 1997; for complete end member ranges see references in the discussion).

nitrite (NO_2^-) then to nitrous oxide (N_2O) under suboxic conditions—result in heavy sedimentary $\delta^{15}N$ values (~5 to 30‰) (e.g., Cline and Kaplan, 1975; Liu and Kaplan, 1989). We therefore do not believe that denitrification influenced our record. Bulk $\delta^{15}N$ values can be affected by microbial ^{14}N remineralization giving rise to organic matter oxidation, increasing $\delta^{15}N$ values of the organic fraction up to +4‰ (e.g., Altabet and François, 1994; Sachs and Repeta, 1999). Still, the parallel $\delta^{15}N$ and TN records, combined with TOC values >0.5% (Fig. 7), exclude the presence of well-ventilated deep-water conditions, suggesting that remineralization was probably minor. Our $\delta^{15}N$ values therefore record both terrestrial-derived organic contributions and nutrient utilization by marine phytoplankton (Fig. 9).

5.2.2. *Molecular (n-alkane) source indicators*

5.2.2.1. CPI values. In order to further characterize the organic matter composition, we used the long chain *n*-alkanes as a proxy for organic matter sources. CPI values >3 and the odd-over-even preference index of long chain *n*-alkanes (i.e., *n*-C_{25} to *n*-C_{34}) are predominantly indicative of terrestrial organic matter (Rieley et al., 1991; Hedges and Prahl, 1993), whereas CPI values around 1 correspond to higher inputs owing to marine microorganisms and/or organic matter recycled by microbial degradation or exposure to elevated burial temperatures (Grimalt et al., 1985; Kennicutt et al., 1987). Longer chain *n*-alkanes are more resistant to degradation by microorganisms, and rates of degradation increase with rising temperatures (e.g., Coulon et al., 2005). Also, *n*-alkanes from petrogenic (diagenetic) inputs have CPI values close to 1 and below (e.g., Farrington and Tripp, 1977). The *n*-Alkane distributions from Hole 696B show a bimodal pattern suggesting two primary sources (*Supplementary Fig. S3*): (1) algae and bacteria as the likely source for the shorter chain lengths, (2) terrestrial higher plants for the longer chain lengths (e.g., Cranwell, 1973; Rieley et al., 1991; Ficken et al., 2000; Bi et al., 2005; Vogts et al., 2009). CPI values are higher than 1, ruling out in situ thermal maturation or upward hydrocarbon migration, in agreement with the identification of well-preserved sporomorph assemblages (Mohr, 1990, 2001). Moreover, old hydrocarbon residues were not recovered (Barker et al., 1988).

5.2.2.2. ACL values. The ACL index can be used as a proxy for input of terrestrial-derived organic matter, though it also reflects changes in climate conditions. Plants produce higher ACL in temperate climates, hence lower ACL in cooler climates (e.g., Poynter et al., 1989; Jeng, 2006; Vogts et al., 2009; Bush and McInerney, 2015). Others authors suggest that plants synthetize longer *n*-alkanes under arid conditions to prevent water loss (Schefuß et al., 2003; Calvo et al., 2004; Moossen et al., 2015). In the study site, ACL values (see Table 1 and Fig. 8; *Supplementary Table S2*) are at the lower end of the range reported for deciduous angiosperms and conifers (e.g., Diefendorf et al., 2011; Diefendorf and Freimuth, 2017). At Hole 696B, higher ACLs suggest a mixed input from higher land-plants generally synthesized under warmer climate conditions, as reported in other paleo-studies (e.g., Jeng, 2006; Vogts et al., 2009; Bush and McInerney, 2015).

5.2.2.3. Paq (aquatic plant n-alkane index). This index serves to discern the relative sedimentary contribution of submerged and floating macrophytes versus emergent aquatic and terrestrial vegetation (Ficken et al., 2000). Yet, *Sphagnum* species (mosses) display molecular distributions similar to those of submerged and floating macrophytes, being characterized by a dominance of *n*-C_{23} and/or *n*-C_{25} (e.g., Baas et al., 2000; Nott et al., 2000; Nichols et al., 2006). At Hole 696B, P*aq* < 0.23 would indicate a dominance of terrestrial plant waxes, and values in the range from 0.48 to 0.49 suggest enhanced contributions by submerged and floating macrophyte and/or *Sphagnum* (Fig. 8; *Supplementary Table S2*).

5.2.2.4. TI (terrestrial n-alkanes index). This index is established on the same assumption as the terrigenous/aquatic ratio (TAR) introduced by Bourbonniere and Meyers (1996), used to reflect the relative input of *n*-$C_{27+29+31}$-rich molecules in vascular plants, but the TI index is calculated as a ratio of $\Sigma C_{27+29+31}$ over TOC (De Mahiques et al., 2017). At the study site, higher values of TI denote a higher input of terrestrial plant-derived organic matter, in agreement with average values of total terrestrial palynomorphs (Houben, 2012) (Fig. 8).

5.3. *Organic matter preservation: Paleoclimatic and paleoceanographic implications*

5.3.1. *Paleoclimatic implications*

During the late Eocene, sediments (Facies IV and III) accumulated with a relatively low TOC content and an overall upward-decreasing trend in CPI, ACL, P*aq* and *n*-C_{29} (*n*-C_{29}/*n*-C_{27} ratio), possibly reflecting mixed input from aquatic plants and certain higher land plants (i.e., deciduous angiosperms and conifers; e.g., Diefendorf and Freimuth, 2017) that commonly characterize relatively humid temperate forests (e.g., Vogts et al., 2009). The presence of the paratropical taxa Arecaceae (palms) along with other warmth-loving taxa (e.g., *Beauprea*, Davalliaceae and Myrtaceae) further indicate warm temperate conditions, and perhaps the absence of winter frosts, given the frost sensitivity of extant palms (Larcher and Winter, 1981; Tomlinson, 2006; Eiserhardt et al., 2011; Reichgelt et al., 2018). This trend is accompanied by upward-decreasing inputs of terrestrial plant-derived organic matter, as reflected by a slight decrease in average TI values (Table 1). The decrease in TI values in Facies III is accompanied by an upward decrease in the total content of terrestrial palynomorphs (Houben, 2012) (Fig. 8). This decreasing trend coincides with large-scale changes in flora composition and diversity on land after ~35.5 Ma, interpreted as recording the onset of prolonged cooling in the Antarctic Peninsula (e.g., Askin, 2000; Anderson et al., 2011; Warny and Askin, 2011).

A larger diversity in angiosperm pollens in sediments from facies IV and within facies III attest to the prevalence of temperate conditions favorable for the growth of *Nothofagus*/conifer forests with an admixture of Proteaceae (Mohr, 1990, 2001). Such diversity has also been reported in coeval southern South American floras (e.g., Romero and Zamaloa, 1985; Romero and Castro, 1986), although leaf impressions in Seymour Island suggest a cool temperate flora (e.g., Case, 1988; Case and Woodburne, 1988). Paleoclimatic conditions recorded in facies IV to III were thus —most probably— intermediate between those in South America/Australasia and the Antarctic Peninsula.

In the latest Eocene, sediments deposited during the two regressive phases within Facies II display an inverse correlation between higher ACL and lower P*aq* values (Fig. 8; *Supplementary Fig. S4*). Together with higher TI values and a higher terrestrial palynomorph content (Fig. 8), they point to higher inputs of terrestrial plant-derived organic matter, but caution is called for because the sediment has been reworked.

Our organic proxies and number of terrestrial palynomorphs exhibit an overall decreasing yet variable pattern before the EOT. Further work is needed to determine if these variations are related to moisture changes, leading to periods of drought as reported in the Antarctic Peninsula (Hosking and Hutcheson, 1988; Suarez et al., 2004). The shift in the trends of some organic matter indices (such as ACL, P*aq* or *n*-C_{29}/*n*-C_{27}) across the EOT and after the time of Oi-1 (Fig. 8) might be associated with the return to near-Eocene climates shortly after the EOT (Liu et al., 2009; Wilson et al., 2013).

In the early Oligocene (from Facies II to I), *n*-C_{27} became the dominant molecule at Hole 696B (e.g., *n*-C_{29}/*n*-C_{27} and *n*-C_{27}/*n*-C_{31} ratios; Fig. 8). Such a change has been attributed to a gradual shift to lowly diverse treeless settings, with vegetation dominated by *Nothofagus* between the Late Eocene and the Oligocene in the Ross Sea region of Antarctica (Duncan et al., 2019). A number of studies on Antarctic material record a shift to treeless low diversity, with stunted *Nothofagus*, podocarpidites and bryophytes (e.g., Askin, 2000; Askin and Raine, 2000; Mohr, 2001; Prebble et al., 2006). Relatively lower ACL values (Fig. 8; *Supplementary Fig. S4*) would also suggest dominance by herbaceous plants and/or conifers, suggesting dry, cool forests. In contrast to these onshore vegetation patterns, increasing P*aq* values suggest an overall increased contribution of submerged/floating plants and/or *Sphagnum* throughout the early Oligocene (Fig. 8). Increased *Sphagnum* input is supported by the moss (bryophyte) spore record at the site (Mohr, 2001), and by relatively higher abundances of *n*-C_{23} (e.g., *n*-C_{23}/*n*-C_{29} ratio; Fig. 8). Such changes would be in agreement with: (1) a general decrease in TI values (Fig. 8; *Supplementary Fig. S4*), indicative of decreased inputs of terrestrial plant-derived organic matter; and (b) a decrease in average terrestrial palynomorphs (Houben, 2012) (Fig. 8).

The *n*-alkane distribution pattern in the upper part of Facies I exhibits trends comparable to those discussed for the latest Eocene, with a major input of terrestrial plant-derived organic matter and increased terrestrial palynomorphs (Fig. 8). However, pollen floras recorded a shift in plant communities due to climate cooling (Mohr, 2001) (Fig. 8).

5.3.2. Paleoceanographic conditions

Two models are frequently used to explain the deposition of organic matter-rich sediments in ocean basins: the stagnation model (silled basins) and the productivity model (upwelling regions) (Demaison and Moore, 1980; Pedersen and Calvert, 1990; Murphy et al., 2000; Harris, 2005; Schoepfer et al., 2015). The stagnation model assumes deposition under a stratified water mass, with prolonged stagnation causing bottom waters to become suboxic or anoxic beneath a permanent halocline or other density contrast. The productivity model assumes that upwelling of nutrient-rich deep water leads to high primary productivity, so that the decay of organic matter settling through the water column consumes oxygen, triggering development of oxygen-deficient bottom waters. In open oceans, mid-water oxygen-depleted zones intersect the continental slope (e.g., Helly and Levin, 2004; Rabalais et al., 2010; Falkowski et al., 2011; Limburg et al., 2020). In addition, major marine ecosystem responses during the Cenozoic have been associated with warm climates and oxygen-deficient oceans (e.g., Norris et al., 2013, and references therein). A fairly broad consensus is emerging in the sense that present day ocean deoxygenation may generally intensify due to global ocean warming (e.g., Falkowski et al., 2011; Schmidtko et al., 2017; Breitburg et al., 2018), especially in continental margin upwelling systems (e.g., Sydeman et al., 2014; Wang et al., 2015; Bakun, 2017).

Sediment facies and ichnological interpretations at Hole 696B point to somewhat shallow-water and reduced-oxygen conditions (Facies IV to III) (Barker et al., 1988; López-Quirós et al., 2019) and recurrent reoxygenation (Facies II to I). Marine condensed glaucony-bearing sections frequently occur beneath high productivity upwelling areas on outer shelf/upper slope environments (e.g., Cook and Marshall, 1981; Wigley and Compton, 2006; Banerjee et al., 2016), and the Fe-enrichment in upper Eocene glaucony grains of Facies III probably resulted from high biological productivity induced by regional nutrient-rich upwelling along the SOM shelf margin (López-Quirós et al., 2019).

Further evidence of changes in the paleoenvironmental conditions and marine biological productivity at Hole 696B comes from the distribution patterns of dinocysts (peridinioids versus gonyaulacoid) and dinocyst feeding strategies. Highly saline, shelf environments tend to feature predominantly heterotroph peridinioid dinocysts, whereas oceanic slope to bathyal environments are dominated by mostly autotroph gonyaulacoid dinocysts. Some peridinioids may be abundant in upwelling-influenced areas (e.g., Dale, 1996; Sluijs et al., 2003, 2005; Röhl and Schmid-Röhl, 2004; Crouch and Brinkhuis, 2005; Pross and Brinkhuis, 2005; Houben et al., 2013, 2019). At Hole 696B, the dominance of peridinioid over gonyaulacoid dinocysts occurs in the late Eocene-early Oligocene, with increased abundance of the genus *Brigantedinium spp.* (Houben et al., 2013, 2019) (see Fig. 7), suggesting eutrophic surface waters above relatively deep (hundreds of meters) shelf waters. The prevalence of such fauna supports the hypothesis that there were highly productive waters at Site 696, with productivity enhanced by upwelling, causing the development of an oxygen-depleted zone intersecting the continental slope (Fig. 10A).

We suggest that the study area was located in a shallow-water flow pathway through the proto-Powell Basin south of the SOM since deposition of Facies III at ~35.5 Ma (Fig. 10B). An upwelling system brought nutrient-rich deep waters to the surface at the SOM shelf margin, fueling high primary productivity throughout the late Eocene and attaining full development by the early Oligocene. As a result, a mid-water oxygen-depleted zone linked to the upwelling was established (Fig. 10A). In addition to the direct physical forcing of paleocirculation, there may have been indirect geochemical effects due to the onset of continental-scale glaciation of Antarctica at the EOT (Zachos et al., 2001; DeConto and Pollard, 2003; Coxall et al., 2005; Lear et al., 2008; Liu et al., 2009; Bohaty et al., 2012). The increased weathering by ice sheets would have increased the flux of fine-grained terrigenous material containing nutrients to the ocean, thus stimulating productivity (e.g., Martin, 1990, 1991).

6. Conclusions

The progressive geographic isolation and deepening of the SOM following the opening of the proto-Powell Basin occurred in four phases under specific paleoenvironmental conditions: (1) ~37.6–35.5 Ma, (2) ~35.5–34.1 Ma, (3) ~34.1–33.6 Ma, and (4) ~33.6–33.2 Ma.

1. During the late Eocene (~37.6–35.5 Ma), prior to the opening of the proto-Powell Basin, the SOM shelf was still attached to the Antarctica Peninsula while sandy mudstones (Facies IV) deposited; however, no evidence of long-distance sediment transport were observed. In contrast, sedimentological and palynological evidences suggest that a significant proportion of detrital material was likely of local origin (e.g., exposed parts of the SOM). Abundant calcareous fauna and ichnological data indicate temperate and reduced-oxygen/salinity conditions in a shallow-water environment.
2. During the latest Eocene (~35.5–34.1 Ma), glauconitic packstone deposition in the outer SOM shelf (Facies III) indicates low sedimentation rates and recurrent bottom-current winnowing under suboxic seafloor conditions. Sedimentation of a condensed section was driven by the shutdown of terrigenous delivery to Site 696 at ~35.5 Ma due to the continuous deepening of the SOM, caused by ongoing rifting and opening of the proto-Powell Basin.
3. At the EOT (~34.1–33.6 Ma), silty mudstone deposition (Facies II) reflects a continuous deepening of the SOM shelf, which was however interrupted by two regressive phases, seen in coarsening-upward layers that record the first arrival of IRD. Sediment facies indicate enhanced oxygenation. The regressive events took place during the EOT, hence the regressive phases probably resulted from continental ice expansion to coastal and shelf areas in response to major cooling.
4. During the early Oligocene (~33.6–33.2 Ma), claystone/clayey mudstones (Facies I) document further deepening of the SOM shelf and enhancement of biological production, partially driven by upwelling along the SOM shelf.

The input of organic matter from marine and terrestrial sources at Hole 696B varied throughout the studied interval because of climatic and tectonic changes. Terrestrial vegetation shifted from humid temperate forests in the late Eocene to dry and cool forests in the early Oligocene, owing to Antarctic cooling. This implies a lesser contribution of terrestrial organic matter to marine sediments, also influenced by progressive deepening of the basin. In addition, the opening of the Powell Basin and the eastward translation of the SOM could have provided a shallow pathway for water flowing towards the northern Weddell Sea, enhancing upwelling at the southern margin of the SOM shelf. We postulate that a system of upwelling —possibly driven and enhanced

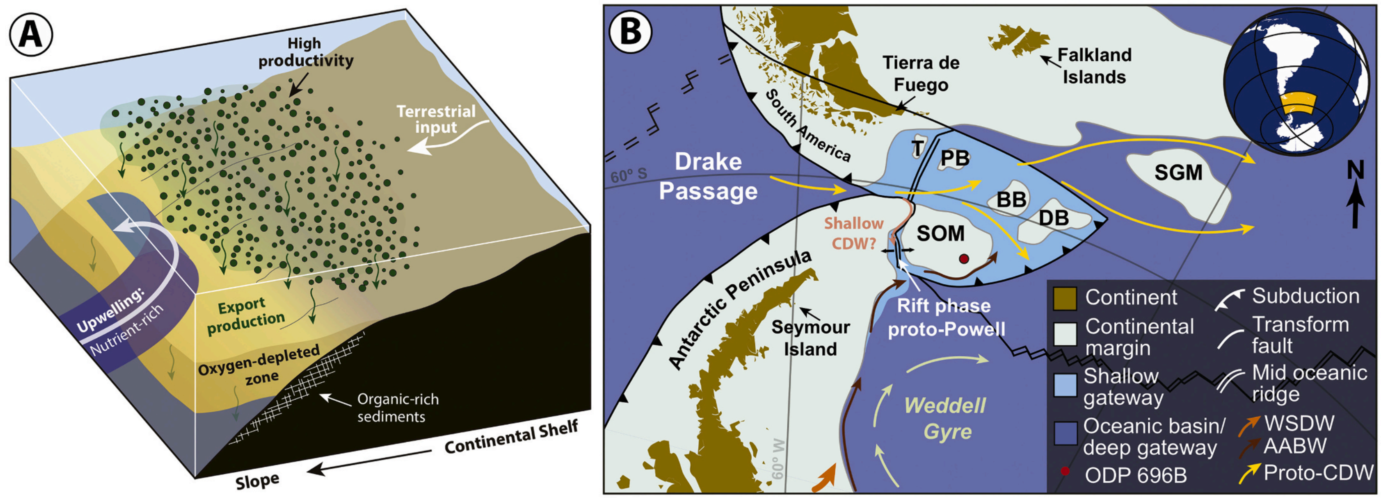

Fig. 10. Paleoceanographic and paleogeographic reconstructions deduced from the preset study at the Eocene-Oligocene transition (EOT ~34 Ma). A) 3-D depositional model involving organic-rich deposition in the shallow-water epicontinental Eötvös Basin during sustained sea-level rise conditions. Upwelled nutrient-rich deep waters led to high productivity in surface waters, while organic matter settling through the water column triggered a mid-water oxygen-depleted zone intersecting the continental slope. B) Paleogeographic reconstruction at the EOT (~34 Ma) around the Drake Passage-Scotia Sea, with the estimated location of the South Orkney Microcontinent (SOM) and ODP Site 696. Plate reconstruction adapted from GPlate software (Boyden et al., 2011). Structural features displayed in the map are adapted from Eagles and Jokat (2014) and references therein. T: Terror Bank; PB: Pirie Bank; BB: Bruce Bank; DB: Dove Bank; SGM: South Georgia Microcontinent; WSDW: Weddell Sea Deep Water; AABW: Antarctic Bottom Water; CDW: Circumpolar Deep Water.

by intensified wind circulation, bringing nutrient-rich deep waters to the surface and fueling high primary productivity— was established in the late Eocene, and fully developed by the early Oligocene. The high productivity led to a mid-water oxygen-depleted zone. Productivity variations since the EOT might have resulted from the combined effects of global and regional cooling, and the tectonic opening of Powell Basin.

Declaration of Competing Interest

The authors declare that they have no known competing financial interests or personal relationships that could have appeared to influence the work reported in this paper.

Acknowledgments

This research relied on samples provided by the International Ocean Discovery Program (IODP). We thank the staff at the Gulf Coast core repository (GCR) for assistance in ODP Leg 113 core handling and shipping. We also acknowledge the help of Dr. Rocío Márquez Crespo (Scientific Instrumentation Center, University of Granada) for her assistance using the ESEM. Thanks are given to Dr. Claus-Dieter Hillenbrand (British Antarctic Survey) for critical reading of an earlier version of this paper, and to Carlos Expósito-Ceballos (University of Granada) for helpful discussions about benthic foraminifera preservation at Hole 696B. We also appreciate the constructive comments provided by Dr. Ellen Thomas and Dr. Sandra Passchier that greatly improved the manuscript. We thank Jean Sanders for correction of the English text. Funding for this research was provided by the Spanish Ministry of Science and Innovation (grants CTM2014-60451-C2-1/2-P and CTM2017-89711-C2-1/2-P) cofounded by the European Union through FEDER funds. RT acknowledges funding provided by Project PID2019-104625RB-100 (Secretaría de Estado de I + D + I, Spain), B-RNM-072-UGR18 (FEDER Andalucía), and P18-RT-4074 (Junta de Andalucía). NT received funding from the Natural Environment Research Council (NERC)-funded Doctoral Training Partnership ONE Planet [NE/S007512/1]. The European Research Council under the European Community's Seventh Framework Program provided funding for this work through ERC Starting Grant #802835 (OceaNice) to PKB. This paper is a contribution to the SCAR PAIS Programme.

Appendix A. Supplementary data

Supplementary data to this article can be found online at https://doi.org/10.1016/j.gloplacha.2021.103581.

References

Altabet, M.A., François, R., 1994. Sedimentary nitrogen isotopic ratio as a recorder for surface ocean nitrate utilization. Glob. Biogeochem. Cycles 8, 103–116.

Amorosi, A., 1995. Glaucony and sequence stratigraphy: a conceptual framework of distribution in siliciclastic sequences. J. Sediment. Res. 65, 419–425.

Amorosi, A., 1997. Detecting compositional, spatial and temporal attributes of glaucony: a tool for provenance research. Sediment. Geol. 109, 135–153.

Amorosi, A., 2012. The occurrence of glaucony in the stratigraphic record: distribution patterns and sequence stratigraphic significance. Int. Assoc. Sedimentol. Spec. Publ. 45, 37–54.

Anderson, J.M., Warny, S., Askin, R.A., Wellner, J.S., Bohaty, S.M., Kirshner, A.E., Livsey, D.N., Simms, A.R., Smith, T.R., Ehrmann, W., Lawver, L.A., Barbeau, D., Wise, S.W., Kulhenek, D.K., Weaver, F.M., Majewski, W., 2011. Progressive Cenozoic cooling and the demise of Antarctica's last refugium. Proc. Natl. Acad. Sci. 108, 11299–11726.

Arbi, I., Liu, S., Zhang, J., Wu, J., Huang, X., 2018. Detection of terrigenous and marine organic matter flow into a eutrophic semi-enclosed bay by δ^{13}C and δ^{15}N of intertidal macrobenthos and basal food sources. Sci. Total Environ. 613, 847–860.

Arndt, J.E., Schenke, H.W., Jakobsson, M., Nitsche, F.O., Buys, G., Goleby, B., Rebesco, M., Bohoyo, F., Hong, J., Jenny Black, J., Greku, R., Udintsev, G., Barrios, F., Reynoso-Peralta, W., Taisei, M., Wigley, R., 2013. The International Bathymetric Chart of the Southern Ocean (IBCSO) Version 1.0—a new bathymetric compilation covering circum-Antarctic waters. Geophys. Res. Lett. 40 (12), 3111–3117.

Askin, R.A., 2000. Spores and pollen from the McMurdo Sound erratics, Antarctica. In: Stilwell, J.D., Feldmann, R.M. (Eds.), Paleobiology and Paleoenvironments of Eocene Fossiliferous Erratics, McMurdo Sound, East Antarctica. AGU Ant. Res. Series, vol. 76, pp. 161–181.

Askin, R.A., Raine, J.I., 2000. Oligocene and early Miocene Terrestrial Palynology of the Cape Roberts Drillhole CRP-2/2A, Victoria Land Basin, Antarctica. Terra Antarct. 7, 493–501.

Baas, M., Pancost, R., van Geel, B., Sinninghe Damsté, J.S., 2000. A comparative study of lipids in Sphagnum species. Org. Geochem. 31, 535–541.

Bakun, A., 2017. Climate change and ocean deoxygenation within intensified surface-driven upwelling circulations. Phil. Trans. R. Soc. A 375, 20160327.

Banerjee, S., Chattoraj, S.L., Saraswati, P.K., Dasgupta, S., Sarkar, U., 2012. Substrate control on formation and maturation of glauconites in the Middle Eocene Harudi Formation, western Kutch, India. Mar. Pet. Geol. 30 (1), 144–160.

Banerjee, S., Bansal, U., Pande, K., Meena, S.S., 2016. Compositional variability of glauconites within the Upper cretaceous Karai Shale Formation, Cauvery Basin, India: Implications for evaluation of stratigraphic condensation. Sediment. Geol. 331, 12–29.

Barker, P.F., 2001. Scotia Sea regional tectonic evolution: implications for mantle flow and palaeocirculation. Earth Sci. Rev. 55, 1–39.

Barker, P.F., Burrell, J., 1977. The opening of Drake Passage. Mar. Geol. 25, 15–34.

Barker, P.F., Thomas, E., 2004. Origin, Signature and Palaeoclimatic Influence of the Antarctic Circumpolar current. Earth Sci. Rev. 66, 143–162.

Barker, P.F., Kennett, J.P., Party, Shipboard Scientific, 1988. Proceedings of the Ocean Drilling Program, Initial Reports, 113. Ocean Drilling Program, College Station, Texas.

Barker, P.F., Dalziel, I.W.D., Storey, B.C., 1991. Tectonic evolution of the Scotia Arc region. In: Tingey, R.J. (Ed.), Antarctic Geology. Oxford Univ Press, pp. 215–248.

Basak, C., Martin, E.E., 2013. Antarctic weathering and carbonate compensation at the Eocene–Oligocene transition. Nat. Geosci. 6, 121–124.

Bi, X., Sheng, G., Liu, X., Li, C., Fu, J., 2005. Molecular and carbon and hydrogen isotopic composition of n-alkanes in plant leaf waxes. Org. Geochem. 36, 1405–1417.

Bohaty, S.M., Zachos, J.C., Delaney, M.L., 2012. Foraminiferal Mg/Ca evidence for Southern Ocean cooling across the Eocene–Oligocene transition. Earth Planet. Sci. Lett. 317, 251–261.

Bohoyo, F., Galindo-Zaldívar, J., Maldonado, A., Schreider, A.A., Suriñach, E., 2002. Basin development subsequent to ridge-trench collision: the Jane Basin, Antarctica. Mar. Geophys. Res. 23, 413–421.

Bourbonniere, R.A., Meyers, P.A., 1996. Anthropogenic influences on hydrocarbon contents of sediments deposited in eastern Lake Ontario since 1800. Environ. Geol. 28, 22–28.

Boyden, J.A., Müller, R.D., Gurnis, M., Torsvik, T.H., Clark, J.A., Turner, M., Ivey-Law, H., Watson, R.J., Cannon, J.S., 2011. Next-generation plate-tectonic reconstructions using GPlates. Geoinformatics 95–114.

Brandes, J.A., Devol, A.H., 2002. A global marine-fixed nitrogen isotopic budget: implications for Holocene nitrogen cycling. Glob. Biogeochem. Cycles 16 (4), 1120.

Breitburg, D., Levin, L.A., Oschlies, A., Grégoire, M., Chavez, F.P., Conley, D.J., Garçon, V., Gilbert, D., Gutiérrez, D., Isensee, K., Jacinto, G.S., Limburg, K.E., Montes, I., Naqvi, S.W.A., Pitcher, G.C., Rabalais, N.N., Roman, M.R., Rose, K.A., Seibel, B.A., Telszewski, M., Yasuhara, M., Zhang, J., 2018. Declining oxygen in the global ocean and coastalwaters. Science. 359 (6371).

Busetti, M., Zanolla, C., Marchetti, A., 2000. Geological Structure of the South Orkney Microcontinent. Terra Antartica 8 (2), 71–78.

Bush, R.T., McInerney, F.A., 2013. Leaf wax n-alkane distributions in and across modern plants: implications for paleoecology and chemotaxonomy. Geochim. Cosmochim. Acta 117, 161–179.

Bush, R.T., McInerney, F.A., 2015. Influence of temperature and C4 abundance on n-alkane chain length distributions across the Central USA. Org. Geochem. 79, 65–73.

Calvo, E., Pelejero, C., Logan, G.A., De Deckker, P., 2004. Dust-induced changes in phytoplankton composition in the Tasman Sea during the last four glacial cycles. Paleoceanography 19, PA2020. https://doi.org/10.1029/2003PA000992.

Carter, A., Riley, T.R., Hillenbrand, C.-D., Rittner, M., 2017. Widespread Antarctic glaciation during the late Eocene. Earth Planet. Sci. Lett. 458, 49–57.

Case, J.A., 1988. Paleogene floras from Seymour Island, Antarctic Peninsula. Geological Society of American Memoir 169, 523–530.

Case, J.A., Woodburne, M.O., 1988. A new genus of polydolopid marsupial from Antarctica. Geological Society of American Memoir 169, 505–521.

Chattoraj, S.L., 2016. Glauconite in Stratigraphic Framework of Palaeogene of Kutch. Lambert Academic Publishing, Saarbrücken, Germany, India (ISBN: 978-3-659-97455-7).

Chattoraj, S.L., Banerjee, S., Saraswati, P.K., 2009. Glauconites from the late palaeocene-early eocene naredi formation, western kutch and their genetic implications. J. Geol. Soc. India 73, 567–574.

Cline, J.D., Kaplan, I.R., 1975. Isotopic fractionation of dissolved nitrate during denitrification in the eastern tropical North Pacific Ocean. Mar. Chem. 3, 271–299.

Clowes, C.D., 1985. Stoveracysta, a new gonyaulacacean dinoflagellate genus from the upper Eocene and lower Oligocene of New Zealand. Palynology 9, 27–35.

Cook, P.J., Marshall, J.F., 1981. Geochemistry of iron and phosphorus-rich nodules from the East Australian continental shelf. Mar. Geol. 41, 205–221.

Coren, F., Ceccone, G., Lodolo, E., Zanolla, C., Zitellini, N., Bonazzi, C., Centonze, J., 1997. Morphology, seismic structure and tectonic development of the Powell Basin, Antarctica. J. Geol. Soc. Lond. 154, 849–862.

Coulon, F., Pelletier, E., Gourhant, L., Delille, D., 2005. Effects of nutrient and temperature on degradation of petroleum hydrocarbons in contaminated sub-Antarctic soil. Chemosphere 58, 1439–1448.

Coxall, H.K., Wilson, P.A., Pälike, H., Lear, C.H., Backman, J., 2005. Rapid stepwise onset of Antarctic glaciation and deeper calcite compensation in the Pacific Ocean. Nature 433, 53–57.

Cramer, B.S., Toggweiler, J.R., Wright, J.D., Katz, M.E., Miller, K.G., 2009. Ocean overturning since the late cretaceous: Inferences from a new benthic foraminiferal isotope compilation. Paleoceanography 24, PA4216. https://doi.org/10.1029/2008PA001683.

Cranwell, P.A., 1973. Chain-length distribution of n-alkanes from lake sediments in relation to post-glacial environmental change. Freshw. Biol. 3, 259–265.

Crouch, E.M., Brinkhuis, H., 2005. Environmental change across the Paleocene-Eocene transition from eastern New Zealand: a marine palynological approach. Mar. Micropaleontol. 56, 138–160.

Dale, B., 1996. Dinoflagellate Cyst Ecology: Modeling and Geological Applications. In: Jansonius, J., McGregor, D.C. (Eds.), Palynology: Principles and applications AASP Foundation, 3, pp. 1249–1275.

Dalziel, I.W.D., 1984. Tectonic evolution of a forearc terrane, southern Scotia Ridge. In: Antarctica. Geological Society of America, Special Paper 200 (32pp).

Dalziel, I.W.D., Elliot, D.H., 1971. Evolution of the Scotia arc. Nature 233, 246–252.

De Mahiques, M.M., Hanebuth, T.J.J., Nagai, R.H., Bícego, M.C., Figueira, R.C.L., Sousa, S.H.M., Burone, L., Franco-Fraguas, P., Taniguchi, S., Salaroli, A.B., Dias, G. P., Prates, D.M., Freitas, M.E.F., 2017. Inorganic and organic geochemical fingerprinting of sediment sources and ocean circulation on a complex continental margin (São Paulo Bight, Brazil). Ocean Sci. 13, 209–222.

De Wit, M.J., 1977. The evolution of the Scotia Arc as a key to the reconstruction of the southwestern Gondwanaland. Tectonophysics 37, 53–81.

DeConto, R.M., Pollard, D., 2003. Rapid Cenozoic glaciation of Antarctica induced by declining atmospheric CO_2. Nature 421 (6920), 245–249.

Demaison, G.J., Moore, G.T., 1980. Anoxic environments and oil source bed genesis. Am. Assoc. Pet. Geol. Bull. 64, 1179–1209.

Diefendorf, A.F., Freimuth, E.J., 2017. Extracting the most from terrestrial plant-derived n-alkyl lipids and their carbon isotopes from the sedimentary record: a review. Org. Geochem. 103, 1–21.

Diefendorf, A.F., Freeman, K.H., Wing, S.L., Graham, H.V., 2011. Production of n-alkyl lipids in living plants and implications for the geologic past. Geochim. Cosmochim. Acta 75, 7472–7485.

Dorador, J., Rodríguez-Tovar, F.J., 2014. A novel application of digital image treatment by quantitative pixel analysis to trace fossil research in marine cores. PALAIOS 29 (10), 533–538.

Dorador, J., Rodríguez-Tovar, F.J., 2018. High-resolution image treatment in ichnological core analysis: initial steps, advances and prospects. Earth-Science Review 177, 226–237.

Duncan, B., McKay, R., Bendle, J., Naish, T., Inglis, G.N., Moossen, H., Levy, R., Ventura, G.T., Lewis, A., Chamberlain, B., Walker, C., 2019. Lipid biomarker distributions in Oligocene and Miocene sediments from the Ross Sea region, Antarctica: Implications for use of biomarker proxies in glacially influenced settings. Palaeogeogr. Palaeoclimatol. Palaeoecol. 516, 71–89.

Dunham, R.J., 1962. Classification of carbonate rocks according to depositional texture. In: Ham, W.E. (Ed.), Classification of Carbonate Rocks, A Symposium. American Association of Petroleum Geology Memoir, vol. 1, pp. 108–121.

Eagles, G., Jokat, W., 2014. Tectonic reconstructions for paleobathymetry in drake passage. Tectonophysics 611, 28–50.

Eagles, G., Livermore, R.A., 2002. Opening history of Powell Basin, Antarctic Peninsula. Mar. Geol. 185, 195–205.

Eagles, G., Livermore, R.A., Morris, P., 2006. Small basins in the Scotia Sea: the Eocene Drake Passage gateway. Earth Planet. Sci. Lett. 242, 343–353.

Egan, K.E., Rickaby, R.E.M., Hendry, K.R., Halliday, A.N., 2013. Opening the gateways for diatoms primes Earth for Antarctic glaciations. Earth Planet. Sci. Lett. 375, 34–43.

Ehrmann, W.U., Mackensen, A., 1992. Sedimentological evidence for the formation of an East Antarctic ice sheet in Eocene/Oligocene time. Palaeogeogr. Palaeoclimatol. Palaeoecol. 93, 85–112.

Eiserhardt, W.L., Svenning, J.-C., Kissling, W.D., Balslev, H., 2011. Geographical ecology of the palms (Arecaceae): determinants of diversity and distributions across spatial scales. Ann. Bot. 108, 1391–1416.

Ekdale, A.A., Mason, T.R., 1988. Characteristic trace-fossil associations in oxygen-poor sedimentary environments. Geology 16, 720–723.

Elliot, D.H., 1988. Tectonic setting and evolution of the James Ross Basin, Northern Antarctic Peninsula. In: Geology and Paleontology of Seymour Island, Antarctic Peninsula (eds RM Feldmann and MO Woodburne). Geological Society of America, Boulder, Colorado, pp. 541–555. Memoir no. 169.

Escutia, C., Brinkhuis, H., Klaus, A., the Expedition 318 Scientists, 2011. Wilkes Land Glacial history: Cenozoic East Antarctic Ice Sheet evolution from Wilkes Land margin sediments. In: Proceedings of the Integrated Ocean Drilling Program, Volume 318. Integrated Ocean Drilling Program Management International Inc., Tokyo https://doi.org/10.2204/iodp.proc.318.2011.

Escutia, C., Brinkhuis, H., Expedition 318 Science Party, 2014. From Greenhouse to Icehouse at the Wilkes Land Antarctic margin: IODP 318 synthesis of results. Pp. 295–328 in Earth and Life Processes Discovered from Subseafloor Environment. In: Stein, R., Blackman, D., Inagaki, F., Larsen, H.C. (Eds.), Developments in Marine Geology, vol. 7, 10.1016/B978–0–444-62617-2.00012-8.

Espitalié, J., Laporte, J.L., Madec, M., Marquis, F., Leplat, P., Paulet, J., Boutefeu, A., 1977. Méthode rapide de characterisation des roches mères, de leur potential pétrolier et de leur degré d'évolution. Revue de l'Institut Francais du Pétrole 32, 23–42.

Exon, N.J., Kennett, J.P., Malone, M., 2001. ODP Leg 189 initial results. In: Proceedings of the ocean drilling program, initial reports of the ODP, p. 189. College Station, TX, USA.

Falkowski, P.G., Algeo, T., Codispoti, L., Deutsch, C., Emerson, S., Hales, B., Huey, R.B., Jenkins, W.J., Kump, L.R., Levin, L.A., Lyons, T.W., Nelson, N.B., Schofield, O.S., Summons, R., Talley, L.D., Thomas, E., Whitney, F., Pilcher, C.B., 2011. Ocean deoxygenation: past, present, and future. Eos 92, 409–410.

Farrington, J.W., Tripp, B.W., 1977. Hydrocarbons in western North Atlantic surface sediments. Geochim. Cosmochim. Acta 41, 1627–1641.

Ficken, K.J., Li, B., Swain, D.L., Eglinton, G., 2000. An n-alkane proxy for the sedimentary input of submerged/floating freshwater aquatic macrophytes. Org. Geochem. 31, 745–749.

Flowerdew, M.J., Riley, T.R., Haselwimmer, C.E., 2011. Geological Map of the South Orkney Islands (1:1 50 000 scale). In: BAS GEOMAP 2 Series, Sheet 3. British Antarctic Survey, Cambridge.

Francis, J.E., Ashworth, A., Cantrill, D.J., Crame, J.A., Stephens, R., Tosolini, A.-M., Thorn, V., 2008. 100 million years of Antarctic climate evolution: evidence from fossil plants. In: Cooper, A.K., Barrett, P.J., Stagg, H., Storey, B., Stumb, E., Wise, W., the 10th ISAES editorial team (Eds.), Antarctica: A Keystone in a Changing World.

Proceedings of the 10th International Symposium on Antarctic Earth Sciences, Washington, D.C., pp. 19–27.

Francis, J.E., Marenssi, S., Levy, R., Hambrey, M., Thorn, V.C., Mohr, B., Brinhkuis, H., Warnaar, J., Zachos, J.C., Bohaty, S.M., DeConto, R.M., 2009. From Greenhouse to Icehouse - the Eocene/Oligocene in Antarctica. In: Florindo, F., Siegert, M. (Eds.), Antarctic CLimate Evolution. Elsevier, Amsterdam, pp. 309–368.

Freeman, K.H., Wakeham, S.G., Hayes, J.M., 1994. Predictive isotopic biogeochemistry: hydrocarbons from anoxic marine basins. Org. Geochem. 21, 629–644.

Gersonde, R., Burckle, L.H., 1990. Neogene Diatom biostratigraphy of ODP Leg 113, Weddell Sea Antarctic Ocean. In: Barker, P.F., Kennett, J.P., et al. (Eds.), Proceeding of the Ocean Drilling Program, Scientific results, Leg 113, volume 113. Ocean Drilling Program, pp. 761–789. College Station, Texas.

Giresse, P., Wiewiora, A., 2001. Stratigraphic condensed deposition and diagenetic evolution of green clay minerals in deep water sediments on the Ivory Coast-Ghana Ridge. Mar. Geol. 179, 51–70.

Grimalt, J., Albaigés, J., Al-Saad, H.T., Douabul, A.A.Z., 1985. n-Alkane distributions in surface sediments from the Arabian Gulf. Naturwissenschaften 72 (1), 35–37.

Hammer, Ø., Harper, D.A.T., Ryan, P.D., 2001. PAST: Paleontological statistics software package for education and data analysis. Palaeontol. Electron. 4 (1), 9.

Harris, N.B., 2005. Deposition of Organic-Carbon-Rich Sediments: Models Mechanisms, and Consequences. SEPM Spec. Publ. 82.

Hedges, J.I., Prahl, F.G., 1993. Early diagenesis: Consequences for applications of molecular biomarkers. In: Macko, S.A. (Ed.), Engel, M.H. Plenum Press, Organic Geochemistry – Principles and Applications, pp. 237–253.

Helly, J.J., Levin, L.A., 2004. Global distribution of naturally occurring marine hypoxia on continental margins. Deep-Sea Research I 51, 1159–1168.

Hosking, G.P., Hutcheson, J.A., 1988. Mountain beech (Nothofagus solandri var. cliffortoides) decline in Kaweka Range, North Island, New Zealand. N. Z. J. Bot. 26, 393–400.

Houben, A.J.P., 2012. Triggers and consequences of glacial expansion across the Eocene-Oligocene transition. Utrecht, the Netherlands. In: LPP Contribution Series No. 39 (Utrecht University).

Houben, A.J., Bijl, P.K., Pross, J., Bohaty, S.M., Passchier, S., Stickley, C.E., Röhl, U., Sugisaki, S., Tauxe, L., van de Flierdt, T., Olney, M., Sangiorgi, F., Sluijs, A., Escutia, C., Brinkhuis, H., the Expedition 318 Scientists, 2013. Reorganization of Southern Ocean plankton ecosystem at the onset of Antarctic glaciation. Science 340 (6130), 341–344.

Houben, A.J.P., Bijl, P.K., Sluijs, A., Schouten, S., Brinkhuis, H., 2019. Late Eocene Southern Ocean cooling and invigoration of circulation preconditioned Antarctica for full-scale glaciation. Geochem. Geophys. Geosyst. 20, 2214–2234.

Huon, S., Grousset, F.E., Burdloff, D., Bardoux, G., Mariotti, A., 2002. Sources of fine-sized organic matter in North Atlantic Heinrich Layers: $\delta^{13}C$ and $\delta^{15}N$ tracers. Geochim. Cosmochim. Acta 66, 223–239.

Jeng, W.L., 2006. Higher plant n-alkane average chain length as an indicator of petrogenic hydrocarbon contamination in marine sediments. Mar. Chem. 102, 242–251.

Jensen, S., Renberg, L., Reutergardh, L., 1977. Residue analysis of sediment and sewage sludge for organochlorines in the presence of elemental Sulphur. Anal. Chem. 49, 316–318.

Jolliffe, I.T., 2002. Principal Component Analysis, 2nd edition. Springer, New York.

Kennett, J.P., 1977. Cenozoic evolution of Antarctic glaciation, the Circum Antarctic Ocean, and their impact on global paleoceanography. J. Geophys. Res. 82, 3843–3860.

Kennicutt, M.C., Barker, C., Brooks, J.M., DeFreitas, D.A., Zhu, G.H., 1987. Selected organic matter source indicators in the Orinoco, Nile and Changjiang deltas. Org. Geochem. 11, 41–51.

King, E.C., Barker, P.F., 1988. The margins of the South Orkney microcontinent. J. Geol. Soc. Lond. 145, 317–331.

Knaust, D., 2012. Trace-fossil systematics. In: Knaust, D., Bromley, R.G. (Eds.), Trace Fossils as Indicators of Sedimentary Environments, Developments in Sedimentology, vol. 64. Elsevier, Amsterdam, pp. 79–101.

Knaust, D., 2017. Atlas of Trace Fossils in Well Core: Appearance, Taxonomy and Interpretation. Springer, Dordrecht, 209 pp.

Lagabrielle, Y., Goddéris, Y., Donnadieu, Y., Malavieille, J., Suarez, M., 2009. The tectonic history of Drake Passage and its possible impacts on global climate. Earth Planet. Sci. Lett. 279, 197–211.

Lamb, A.L., Wilson, G.P., Leng, M.J., 2006. A review of coastal palaeoclimate and relative sea-level reconstructions using $\delta^{13}C$ and C/N ratios in organic material. Earth-Science Review 75, 29–57.

Larcher, W., Winter, A., 1981. Frost suceptibility of palms: experimental data and their interpretation. Principes 25 (143–155), 1981.

Lawver, L.A., Gahagan, L.M., 1998. Opening of Drake Passage and its impact on Cenozoic Ocean circulation. In: Crowley, T.J., Burke, K.C. (Eds.), Tectonic Boundary Conditions for Climate Reconstructions. Oxford Univ. Press, New York, pp. 212–223.

Lawver, L., Gahagan, L.M., 2003. Evolution of Cenozoic seaways in the circum-Antarctic region. Palaeogeogr. Palaeoclimatol. Palaeoecol. 198, 11–37.

Lawver, L.A., Della Vedova, B., Von Herzen, R.P., 1991. Heat flow in Jane Basin, Northern Weddell Sea. J. Geophys. Res. 96 (B2), 2019–2038.

Lear, C.H., Bailey, T.R., Pearson, P.N., Coxall, H.K., Rosenthal, Y., 2008. Cooling and ice growth across the Eocene-Oligocene transition. Geology 36, 251–254.

Limburg, K.E., Breitburg, D., Swaney, D.P., Jacinto, G., 2020. Ocean Deoxygenation: a Primer. One Earth 2, 24–29.

Liu, K.-K., Kaplan, I.R., 1989. Eastern tropical Pacific as a source of ^{15}N-enriched nitrate in seawater off southern California. Limnol. Oceanogr. 34, 820–830.

Liu, Z., Pagani, M., Zinniker, D., DeConto, R., Huber, M., Brinkhuis, H., Shah, S.R., Leckie, R.M., Pearson, A., 2009. Global cooling during the Eocene-Oligocene climate transition. Science 323 (5918), 1187–1190.

Livermore, R.A., Eagles, G., Morris, P., Maldonado, A., 2004. Shackleton Fracture Zone: no barrier to early circumpolar ocean circulation. Geology 32, 797–800.

Livermore, R.A., Hillenbrand, C.D., Meredith, M., Eagles, G., 2007. Drake Passage and Cenozoic climate: an open and shut case? Geochem. Geophys. Geosyst. 8 https://doi.org/10.1029/2005GC001224. Q01005.

López-Quirós, A., Escutia, C., Sánchez-Navas, A., Nieto, F ., García-Casco, A., Martín-Algarra, A., Evangelinos, D., Salabarnada, A., 2019. Glaucony authigenesis, maturity and alteration in the Weddell Sea: an indicator of paleoenvironmental conditions before the onset of Antarctic glaciation. Sci. Rep. 9:13580. https://doi.org/10.1038/s41598-019-50107-1.

López-Quirós, A., Sánchez-Navas, A., Nieto, F., Escutia, C., 2020. New insights into the nature of glauconite. Am. Mineral. 105, 674–686.

Maestro, A., López-Martínez, J., Bohoyo, F., 2013. Mesozoic to recent evolution of intraplate stress fields under multiple remote stresses: the case of Signy Island (South Orkney Microcontinent, Antarctica). Geol. Soc. Lond., Spec. Publ. 381, 45–65.

Maldonado, A., Zitellini, N., Leitchenkov, G., Balanya, J.C., Coren, F., Galindo-Zaldívar, J., Lodolo, E., Jabaloy, A., Zanolla, C., Rodrigues-Fernandez, J., Vinnikovsakya, O., 1998. Small ocean basin development along the Scotia-Antarctica plate boundary and in the northern Weddell Sea. Tectonophysics 296, 371–402.

Maldonado, A., Balanyá, J.C., Barnolas, A., Galindo-Zaldivar, J., Hernández, J., Jabaloy, A., Livermore, R., Martínez-Martínez, J.M., Rodríguez-Fernández, J., De Galdeano, C.S., Somoza, L., Suriñach, E., Viseras, C., 2000. Tectonics of an extinct ridge-transform intersection, Drake Passage (Antarctica). Mar. Geophys. Res. 21 (1–2), 43–67.

Maldonado, M., Bohoyo, F., Galindo-Zaldívar, J., Hernández-Molina, F.J., Lobo, F.J., Lodolo, E., Martos, Y.M., Pérez, L.F., Schreider, A.A., Somoza, L., 2014. A model of oceanic development by ridge jumping: opening of the Scotia Sea. Glob. Planet. Chang. 123, 152–173.

Marenssi, S.A., Santillana, S.N., Rinaldi, C., 1998. Stratigraphy of La Meseta Formation (Eocene), Marambio Island, Antarctica. In: Paleógeno de América del Sur y de la Península Antártica (ed. S Casadío), pp. 137–46. Maipú. Revista de la Asociación Paleontológica Argentina. Publicación Especial no. 5.

Marenssi, S.A., Net, L.I., Santillana, S.N., 2002. Provenance, environmental and paleogeographic controls on sandstone composition in an incised valley system: the Eocene La Meseta Formation, Seymour Island, Antarctica. Sediment. Geol. 150, 301–321.

Martin, J.H., 1990. Glacial–interglacial CO_2 change: the iron hypothesis. Paleoceanography 5 (1), 1–13.

Martin, J.H., 1991. Iron, Liebig's Law, and the greenhouse. Oceanography 4 (2), 52–55.

Meyers, P.A., 1994. Preservation of elemental and isotopic source identification of sedimentary organic matter. Chem. Geol. 144, 289–302.

Meyers, P.A., 1997. Organic geochemical proxies of paleoceanographic, paleolimnologic, and paleoclimatic processes. Org. Geochem. 27, 213–250.

Miguez-Salas, O., Rodríguez-Tovar, F.J., 2019. Ichnofacies distribution in the Eocene-early Miocene Petra Tou Romiou outcrop, Cyprus: sea level dynamics and palaeoenvironmental implications in a contourite environment. Int. J. Earth Sci. 108, 2531–2544.

Miller, K.G., Kominz, M.A., Browning, J.V., Wright, J.D., Mountain, G.S., Katz, M.E., Sugarman, P.J., Cramer, B.S., Christie-Blick, N., Pekar, S.F., 2005. The Phanerozoic Record of Global Sea Level Change, vol. 310. Science, New York, N.Y, pp. 1293–1298.

Minoura, K., Hoshino, K., Nakamura, T., Wada, E., 1997. Late Pleistocene-Holocene paleoproductivity circulation in the Japan Sea: Sea-level control on $d^{13}C$ and $d^{15}N$ records of sediment organic material. Palaeogeogr. Palaeoclimatol. Palaeoecol. 135, 41–50.

Mohr, B.A.R., 1990. Eocene and Oligocene sporomorphs and dinoflagellate cysts from Leg 113 drill sites, Weddell Sea, Antarctica. In: Barker, P.F., Kennett, J.R., et al. (Eds.), Proceedings of the Ocean Drilling Program, Scientific results 113 (pp. 595–612).

Mohr, B.A.R., 2001. The development of Antarctic fern floras during the Tertiary, and palaeoclimatic and palaeobiogeographic implications. Palaeontographica B 259, 167–208.

Moossen, H., Bendle, J., Seki, O., Quillmann, U., Kawamura, K., 2015. North Atlantic Holocene climate evolution recorded by high-resolution terrestrial and marine biomarker records. Quat. Sci. Rev. 129, 111–127.

Mount, J., 1985. Mixed siliciclastic and carbonate sediments: a proposed first-order textural and compositional classification. Sedimentology 32, 435–442.

Muller, A., Voss, M., 1999. The paleoenvironments of coastal lagoons in the southern Baltic Sea, II. D13C and d15N ratios of organic matter – sources and sediments. Palaeogeogr. Palaeoclimatol. Palaeoecol. 145, 17–32.

Murphy, A.E., Sageman, B.B., Hollander, D.J., Lyons, T.W., Brett, C.E., 2000. Black shale deposition in the Devonian Appalachian Basin: siliciclastic starvation, episodic water-column mixing, and efficient recycling of biolimiting nutrients. Paleoceanography 15, 280–291.

Nichols, J.E., Booth, R.K., Jackson, S.T., 2006. Paleohydrologic reconstruction based on n-alkane distributions in ombrotrophic peat. Org. Geochem. 37, 1505–1513.

Norris, R.D., Turner, S.K., Hull, P.M., Ridgwell, A., 2013. Marine ecosystem responses to Cenozoic global change. Science 341, 492–498.

Nott, C.J., Xie, S., Avsejs, L.A., Maddy, D., Chambers, F.M., Evershed, R.P., 2000. N-Alkane distributions in ombrotrophic mires as indicators of vegetation change related to climatic variations. Org. Geochem. 31, 231–235.

Orsi, A.H., Nowlin, W.D., Whitworth, T., 1993. On the circulation and stratification of the Weddell Gyre. Deep-Sea Res. I Oceanogr. Res. Pap. 40 (1), 169–203.

Passchier, S., Krissek, L.A., 2008. Oligocene-Miocene Antarctic continental weathering record and paleoclimatic implications, Cape Roberts drilling project, Ross Sea, Antarctica. Palaeogeogr. Palaeoclimatol. Palaeoecol. 260, 30–40.

Passchier, S., Bohaty, S.M., Jimenez-Espejo, F., Pross, J., Roehl, U., van de Flierdt, T., Escutia, C., Brinkhuis, H., 2013. Early Eocene to middle Miocene cooling and aridification of East Antarctica. Geochem. Geophys. Geosyst. 14, 1399–1410.

Passchier, S., Ciarletta, D.J., Miriagos, T.E., Bijl, P.K., Bohaty, S.M., 2017. An Antarctic stratigraphic record of stepwise ice growth through the Eocene-Oligocene transition. Geol. Soc. Am. Bull. 129 (3–4), 318–330.

Paytan, A., Mearon, S., Cobb, K., Kastner, M., 2002. Origin of marine barite deposits: Sr and S isotope characterization. Geology 30 (8), 747–750.

Pedersen, T.F., Calvert, S.E., 1990. Anoxia vs productivity; what controls the formation of organic-carbon-rich sediments and sedimentary rocks? AAPG Bull. 74 (4), 454–466.

Peters, K.E., Sweeney, R.E., Kaplan, I.R., 1978. Correlation of carbon and nitrogen stable isotope ratios in sedimentary organic matter. Limnol. Oceanogr. 23, 598–604.

Peterson, B.J., Howarth, R.W., Garritt, R.H., 1985. Multiple stableisotopes used to trace the flow of organic matter in estuarinefood webs. Science 227, 1361–1363.

Poole, I., Cantrill, D., Utescher, T., 2005. A multi-proxy approach to determine Antarctic terrestrial palaeoclimate during the late cretaceous and early Tertiary. Palaeogeogr. Palaeoclimatol. Palaeoecol. 222, 95–121.

Poynter, J.G., Farrimond, P., Robinson, N., Eglinton, G., 1989. Aeolian-derived higher plant lipids in the marine sedimentary record: links with palaeoclimate. In: Paleoclimatology and Paleometeorology: Modern and past patterns of Global Atmospheric Transport. Springer, Netherlands, pp. 435–462.

Prahl, F.G., Bennett, J.T., Carpenter, R., 1980. The early diagenesis of aliphatic hydrocarbons and organic matter in sedimentary particulates from Dabob Bay, Washington. Geochim. Cosmochim. Acta 44, 1967–1976.

Prebble, J.G., Raine, J.I., Barrett, P.J., Hannah, M.J., 2006. Vegetation and climate from two Oligocene glacioeustatic sedimentary cycles (31 and 24 Ma) cored by the Cape Roberts Project, Victoria Land Basin, Antarctica. Palaeogeogr. Palaeoclimatol. Palaeoecol. 231, 41–57.

Pross, J., Brinkhuis, H., 2005. Organic-walled dinoflagellate cysts as paleoenvironmental indicators in the Paleogene; a synopsis of concepts. Paläontol. Z. 79 (1), 53–59.

Pross, J., Houben, A.J.P., Simaeys, S., Williams, G.L., Kotthoff, U., Coccioni, R., Wilpshaar, M., Brinkhuis, H., 2010. Umbria–Marche revisited: a refined magnetostratigraphic calibration of dinoflagellate cyst events for the Oligocene of the Western Tethys. Rev. Palaeobot. Palynol. 158, 213–235.

Rabalais, N.N., Díaz, R.J., Levin, L.A., Turner, R.E., Gilbert, D., Zhang, J., 2010. Dynamics and distribution of natural and human-caused hypoxia. Biogeosciences 7, 585–619.

Reichgelt, T., West, C.K., Greenwood, D.R., 2018. The relation between global palm distribution and climate. Sci. Rep. 8 (1), 4721.

Rieley, G., Collier, R.J., Jones, D.M., Eglinton, G., 1991. The biogeochemistry of Ellesmere Lake, U.K.—I: source correlation of leaf wax inputs to the sedimentary lipid record. Org. Geochem. 17, 901–912.

Riis, V., Babel, W., 1999. Removal of sulfur interfering in the analysis of organochlorines by GC-ED. Analyst 124, 1771–1773.

Robert, C., Maillot, H., 1990. Palaeoenvironments in the Weddell Sea area and Antarctic climates, as deduced from clay mineral associations and geochemical data, ODP Leg 113. In: Barker, P.F., Kennett, J.P., et al. (Eds.), Proceedings of the Ocean Drilling Program, pp. 51–66 (Scientific Results 113).

Rodríguez-Tovar, F.J., Puga-Bernabéu, Á., Buatois, L.A., 2008. Large burrow systems in marine Miocene deposits of the Betic Cordillera (Southeast Spain). Palaeogeogr. Palaeoclimatol. Palaeoecol. 268, 19–25.

Rodríguez-Tovar, F.J., Nagy, J., Reolid, M., 2014. Palaeoenvironment of Eocene prodelta in Spitsbergen recorded by the trace fossil *Phycosiphon incertum*. Polar Res. 33, 23786.

Rodríguez-Tovar, F.J., Dorador, J., Grunert, P., Hodell, D., 2015a. Deep-sea trace fossil and benthic foraminiferal assemblages across glacial Terminations 1, 2 and 4 at the 'Shackleton Site' (IODP Expedition 339, Site U1385). Glob. Planet. Chang. 133, 359–370.

Rodríguez-Tovar, F.J., Dorador, J., Martín-García, G.M., Sierro, F.J., Flores, J.A., Hodell, D.A., 2015b. Response of macrobenthic and foraminifer communities to changes in deep-sea environmental conditions from Marine Isotope Stage (MIS) 12 to 11 at the 'Shackleton Site'. Glob. Planet. Chang. 133, 176–187.

Rodríguez-Tovar, F.J., Miguez-Salas, O., Duarte, L.V., 2017. Toarcian Oceanic Anoxic Event induced unusual behaviour and palaeobiological changes in *Thalassinoides* tracemakers. Palaeogeogr. Palaeoclimatol. Palaeoecol. 485, 46–56. https://doi.org/10.1016/j.palaeo.2017.06.002.

Rodríguez-Tovar, F.J., Dorador, J., Hodell, D.A.V., 2019. Trace fossils evidence of a complex history of nutrient availability and oxygen conditions during Heinrich Event 1. Glob. Planet. Chang. 174, 26–34.

Rodríguez-Tovar, F.J., Dorador, J., Mena, A., Francés, G., 2020. Regional and global changes during Heinrich Event 1 affecting macrobenthic habitat: Ichnological evidence of sea-bottom conditions at the Galicia Interior Basin. Glob. Planet. Chang. 192, 103227.

Röhl, H.-J., Schmid-Röhl, A., 2004. Lower Toarcian (Upper Liassic) black shales of the central European epicontinental basin: a sequence stratigraphic case study from the SW German Posidonia Shale. In: Harris NB (ed) the deposition of organic-carbon-rich sediments: models, mechanisms, and consequences. SEPM Spec. Publ. 82, 165–189.

Romero, E.J., Castro, M.T., 1986. Material fungico y granos de polen de angiospermas de la Formacion Rio Turbio (Eoceno), Provincia de Santa Cruz, Republica Argentina. Ameghiniana 23, 101–118.

Romero, E.J., Zamaloa, M.C., 1985. Polen de Angiospermas de la Formacion Rio Turbio (Eoceno), Provincia de Santa Cruz, Republica Argentina. Ameghiniana 22, 43–51.

Sachs, J.P., Repeta, D.J., 1999. Oligotrophy and nitrogen fixation during eastern Mediterranean sapropel events. Science 286, 2485–2488.

Schefuß, E., Ratmeyer, V., Stuut, J.-B.W., Jansen, J.H.F., Sinninghe Damsté, J.S., 2003. Carbon isotope analyses of n-alkanes in dust from the lower atmosphere over the central eastern Atlantic. Geochim. Cosmochim. Acta 67, 1757–1767.

Scher, H.D., Martin, E.E., 2006. Timing and climatic consequences of the opening of the Drake Passage. Science 312, 428–430.

Schmidtko, S., Stramma, L., Visbeck, M., 2017. Decline in global oceanic oxygen content during the past five decades. Nature 542, 335–339.

Schoepfer, S.D., Shen, J., Wei, H.Y., Tyson, R.V., Ingall, E., Algeo, T.J., 2015. Total organic carbon, organic phosphorus, and biogenic bariumfluxes as proxies for paleomarine productivity. Earth-Science Review 149, 23–52.

Simoneit, B.R., Cardoso, J.N., Robinson, N., 1991. An assessment of terrestrial higher molecular weight lipid compounds in aerosol particulate matter over the South Atlantic from about 30–70 S. Chemosphere 23, 447–465.

Sluijs, A., Brinkhuis, H., Stickley, C.E., Warnaar, J., Williams, G.L., Fuller, M., 2003. Dinoflagellate cysts from the eocene-oligocene transition in the Southern Ocean: results from ODP Leg 189. In: Exon, N.F., Kennett, J.P., Malone, M.J. (Eds.), Proceedings of the Ocean Drilling Program, Scientific Results, Volume 189, pp. 1–41.

Sluijs, A., Pross, J., Brinkhuis, H., 2005. From greenhouse to icehouse; organic- walled dinoflagellate cysts as paleoenvironmental indicators in the Paleogene. Earth-Sci. Rev. 68, 281–315.

Stilwell, J., Zinsmeister, W., 1992. Molluscan systematics and biostratigraphy, lower Tertiary La Meseta Formation, Seymour Island, Antarctic Peninsula. Am. Geophys. Union, Antarctic Res. Series 55, 1–192.

Stocchi, P., Escutia, C., Houben, A., Vermeersen, B., Bijl, P., Brinkhuis, H., DeConto, R., Galeotti, S., Passchier, S., Pollard, D., Klaus, A., Fehr, A., Williams, T., Bendle, J.A.P., Bijl, P.K., Bohaty, S.M., Carr, S.A., Dunbar, R.B., Flores, J.A., Gonzàlez, J.J., Hayden, T.G., Iwai, M., Jimenez-Espejo, F.J., Katsuki, K., Kong, G.S., McKay, R.M., Nakai, M., Olney, M.P., Pekar, S.F., Pross, J., Riesselman, C., Röhl, U., Sakai, T., Shrivastava, P.K., Stickley, C.E., Sugisaki, S., Tauxe, L., Tuo, S., van de Flierdt, T., Welsh, K., Yamane, M., 2013. Relative Sea-level rise around East Antarctica during Oligocene glaciation. Nat. Geosci. 6, 380–384.

Suarez, M.L., Ghermandi, L., Kitzberger, T., 2004. Factors predisposing episodic drought-induced tree mortality in Nothofagus—site, climatic sensitivity and growth trends. J. Ecol. 92, 954–966.

Sydeman, W.J., García-Reyes, M., Schoeman, D.S., Rykaczewski, R.R., Thompson, S.A., Black, B.A., S, J., 2014. Climate change and wind intensification in coastal upwelling ecosystems. Science 345, 77–80.

Tissot, B., Welte, D.H., 1984. Petroleum Formation and Occurrence. Springer, Berlin, p. 699.

Tomlinson, P.B., 2006. The uniqueness of palms. Bot. J. Linn. Soc. 151 (1), 5–14.

Tribovillard, N., Algeo, T.J., Lyons, T., Riboulleau, A., 2006. Trace metals as paleoredox and paleoproductivity proxies: an update. Chem. Geol. 232, 12–32.

Trouw, R., Passchier, C., Simoes, L., Andreis, R., Valeriano, C., 1997. Mesozoic tectonic evolution of the South Orkney Microcontinent, Scotia arc, Antarctica. Geol. Mag. 134 (3), 383–401.

Tucker, M.E., 2001. Sedimentary Petrology: An Introduction to the Origin of Sedimentary Rocks. Blackwell Science Ltd., Oxford, 260 pp.

Villa, G., Fioroni, C., Pea, L., Bohaty, S., Persico, D., 2008. Middle Eocene-late Oligocene climate variability: Calcareous nannofossil response at Kerguelen Plateau, Site 748. Mar. Micropaleontol. 69, 171–192.

Villa, G., Fioroni, C., Persico, D., Roberts, A.P., Florindo, F., 2014. Middle Eocene to late Oligocene Antarctic glaciation/deglaciation and Southern Ocean productivity. Paleoceanography 29, 223–237.

Vogts, A., Moossen, H., Rommerskirchen, F., Rullkötter, J., 2009. Distribution patterns and stable carbon isotopic composition of alkanes and alkan-1-ols from plant waxes of African rain forest and savanna C3 species. Org. Geochem. 40, 1037–1054.

Wang, D., Gouhier, T.C., Menge, B.A., Ganguly, A.R., 2015. Intensification and spatial homogenization of coastal upwelling under climate change. Nature 518, 390–394.

Warny, S., Askin, R., 2011. Vegetation and organic-walled phytoplankton at the end of the Antarctic greenhouse world: Latest Eocene cooling events. In: Anderson, J.B., Wellner, J.S. (Eds.), Tectonic, Climatic, and Cryospheric Evolution of the Antarctic Peninsula. American Geophysical Union, Washington, D.C., pp. 193–210

Warny, S., Kymes, C.M., Askin, R., Krajewski, K.P., Tatur, A., 2019. Terrestrial and marine floral response to latest. Eocene and Oligocene events on the Antarctic Peninsula 43 (1), 4–21.

Wei, W., Wise, S.W., 1990. Middle Eocene to Pleistocene calcareous nannofossils recovered by Ocean Drilling Program Leg 113 in the Weddell Sea. In: Proceedings of the Ocean Drilling Program, Scientific results 113, vol. 188. Ocean Drilling Program, College Station, Texas, pp. 639–666.

Wellner, J.S., Anderson, J.B., Ehrmann, W., Weaver, F.M., Kirshner, A., Livsey, D., Simms, A.R., 2011. History of an evolving ice sheet as recorded in SHALDRIL cores from the Northwestern Weddell Sea, Antarctica. In: Anderson, J.B., Wellner, J.S. (Eds.), Tectonic, Climatic, and Cryospheric Evolution of the Antarctic Peninsula. American Geophysical Union, Washington, D.C., pp. 131–152

Wetzel, A., Uchman, A., 2001. Sequential colonization of muddy turbidites in the Eocene Beloveza Formation, Carpathians, Poland. Paleogeography, Palaeoclimatology, Palaeoecology 168, 171–186.

Wigley, R.A., Compton, J.S., 2006. Late Cenozoic evolution of the outer continental shelf at the head of the Cape Canyon, South Africa. Mar. Geol. 226, 1–23.

Wilson, D.S., Pollard, D., DeConto, R.M., Jamieson, S.S., Luyendyk, B.P., 2013. Initiation of the West Antarctic ice sheet and estimates of total Antarctic ice volume in the earliest Oligocene. Geophys. Res. Lett. 40, 4305–4309.

Zachos, J.C., Pagani, M., Sloan, L., Thomas, E., Billups, K., 2001. Trends, rhythms and aberrations in global climate 65 Ma to present. Science 292, 686–693.